POLITECNICO DI TORINO
Repository ISTITUZIONALE

Advanced Current-Controlled Generators Models for Electrically Excited Synchronous Machines

Original
Advanced Current-Controlled Generators Models for Electrically Excited Synchronous Machines / Perilli, L., Rubino, S., Graffeo, F., Vaschetto, S., Tenconi, A.. - In: IEEE OPEN JOURNAL OF INDUSTRY APPLICATIONS. - ISSN 2644-1241. - ELETTRONICO. - 7:(2026), pp. 806-824. [10.1109/ojia.2026.3711705]

Availability:
This version is available at: 11583/3013754 since: 2026-07-30T09:43:58Z

Publisher:
Institute of Electrical and Electronics Engineers Inc.

Published
DOI:10.1109/ojia.2026.3711705

Terms of use:

This article is made available under terms and conditions as specified in the corresponding bibliographic description in the repository

Publisher copyright

(Article begins on next page)

18 November 2026

IEEE Open Journal of
Industry Applications

Received 19 January 2026; revised 8 June 2026; accepted 6 July 2026. Date of publication 9 July 2026;
date of current version 27 July 2026.

Digital Object Identifier 10.1109/OJIA.2026.3711705

Advanced Current-Controlled Generators Models for Electrically Excited Synchronous Machines

LORENZO PERILLI (Student Member, IEEE), SANDRO RUBINO (Senior Member, IEEE), FEDERICA GRAFFEO (Member, IEEE), SILVIO VASCHETTO (Senior Member, IEEE), AND ALBERTO TENCONI

Dipartimento Energia "G. Ferraris," Politecnico di Torino, 10129 Turin, Italy

CORRESPONDING AUTHOR: LORENZO PERILLI (e-mail: lorenzo.perilli@polito.it).

The work of Lorenzo Perilli was supported by the PNRR-NGEU project, funded by the MUR-DM 117/2023. The work of Silvio Vaschetto and Alberto Tenconi was supported by the COMET-K2 "Center for Symbiotic Mechatronics" of the Linz Center of Mechatronics (LCM), funded by the Austrian federal government and the federal state of Upper Austria.

ABSTRACT Electrically excited synchronous machines (EESMs) potentially constitute suitable alternatives to the permanent magnet (PM) counterparts in the context of transportation electrification for the design and manufacturing of sustainable PM-free traction drives. The convenient current regulation enabled by the rotor winding represents the distinguishing feature of the EESMs, allowing the machine performance to be optimized under different operating conditions. Nevertheless, the added complexity introduced by the variable rotor current results in a challenging implementation of high-fidelity dynamic models for numerical simulations. Indeed, the severe magnetic saturation typically exhibited by traction EESMs, including the significant magnetic coupling between the stator and rotor windings, must be accurately taken into account. In this framework, this article proposes advanced EESM models based on a current-controlled generators approach, which allow interdependent simulations of stator and rotor winding dynamics, thus providing enhanced simulation capabilities. Also, multidimensional-map-based formulations are adopted to include the significant saturation nonlinearities, comparing their accuracy and computational burden with the state-of-the-art models. The proposed EESM models have been experimentally validated on a 100 kW commercial EESM sample from an automotive manufacturer, demonstrating their added value in accurately replicating the electromagnetic behavior of the machine in the simulation environment.

INDEX TERMS Current-controlled generators (CCG) model, dynamic modeling, electrically excited synchronous machine (EESM), flux maps, magnetic saturation.

I. INTRODUCTION

Many recent research activities from the academic and industrial contexts have been focusing on electrically excited synchronous machines (EESMs) to develop further advancements oriented toward more sustainable transport electrification [1], [2]. Within this framework, the uncertain availability and wide price oscillations of permanent magnets (PMs), combined with the environmental hazard of the mass extraction for intensive production, have all contributed to the increasing interest in enabling PM-free systems based on EESMs [3], [4]. Some of the most relevant car manufacturers have already adopted EESMs, as well as other sectors, such as the passenger aircraft industry [5].

The peculiarity of the EESMs is represented by the rotor winding, which generates the excitation field [6], [7]. The controllability of the rotor current allows achieving optimal and efficient torque regulation, while enhancing the overall safety of the electric drive [8]. In this regard, the possibility of promptly removing the excitation field in case of faults ensures the complete machine de-energization, differently from the PM machines [9], [10]. In addition, the EESMs are characterized by a large overload torque, high efficiency

© 2026 The Authors. This work is licensed under a Creative Commons Attribution 4.0 License. For more information, see https://creativecommons.org/licenses/by/4.0/

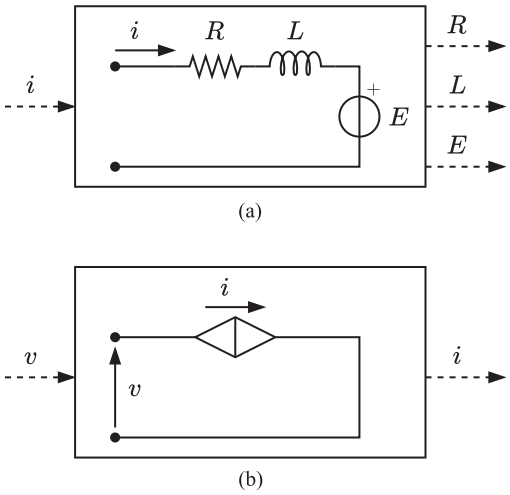


FIGURE 1. Circuital representation of electric machine models. (a) voltage-behind-reactance — VBR. (b) current-controlled generators — CCG.

at partial loads and a wide constant power speed range, all allowed by the rotor current regulation [11], [12]. However, the Joule losses of the rotor winding restrict the obtainable power density and result in a more challenging cooling with respect to the PM machines [13]. Regarding the rotor current supply, brushless systems based on capacitive or inductive couplings have been proposed to reduce maintenance and to improve reliability compared to brushed contacts, especially in high-speed applications [14], [15], [16]. In the aerospace sector, multistage exciters are adopted for safety reasons [17], [18], [19], [20], [21].

As the ongoing studies on EESMs for transportation are advancing, the implementation of simulation models imposes stringent fidelity requirements [22], [23]. Accurate dynamic modeling is demanded for control algorithms development and numerical simulations [24], hardware-in-the-loop testing [25], and real-time condition monitoring of electric machines [26], [27]. For these purposes, the simulation models must represent the magnetic saturation nonlinearities, while also featuring limited computational burden [28], [29]. Moreover, the EESM dynamic modeling is further complicated by the rotor winding, introducing additional variables with respect to the PM machine models [30].

In this context, the research contributions to the nonlinear modeling of EESMs have been primarily oriented to circuit-based simulation approaches [31]. Specifically, these EESM models are developed according to voltage-behind-reactance (VBR) formulations, for convenient integration and analysis with power electronics converters in numerical simulations [32], [33], [34]. In the VBR models, the stator and rotor currents are the inputs, whereas the resistances, inductances, and back-electromotive forces are the outputs, as shown in Fig. 1(a). Saturation curves are defined to approximate the magnetic nonlinearities, providing a relationship between magnetizing current and flux linkage [35], [36], [37]. In order to improve the fidelity of the model in representing the magnetic saturation, current-to-flux maps, i.e., the relationships between machine currents and flux linkages, have been included in the VBR formulation recently proposed in [38].

According to the literature, a potential alternative to VBR modeling is represented by the current-controlled generators (CCG) approaches [39], [40], [41]. The CCG formulation of an electric machine, regardless of whether electrically excited or PM machines are considered, features the terminal voltages as inputs, while the currents are the outputs [42], [43]. This representation leads to a machine circuital scheme based on current-controlled generators, as illustrated in Fig. 1(b). The implementation of accurate CCG models is achieved through different typologies of multidimensional maps [44], [45]. In the state-of-the-art CCG models, an intensive use of maps obtained either by means of finite element analyses or by experimental testing procedures is required [46], [47]. The CCG models can also be classified depending on the type of state-space variables that are considered [48]. In particular, the so-called *current-based* models rely on the computation of the time derivatives of the machine currents. Conversely, the so-called *flux-based* models feature the flux linkages as state-space variables.

Current-based EESM models have been comprehensively investigated for their straightforward implementation through current-to-inductance maps [49], [50], [51]. However, due to the high sensitivity of convergence to the values of incremental inductance, a flux-based EESM model with flux-to-current maps has been proposed in [52] as an alternative approach for state-space-variable-based simulation software, although long and demanding offline computations seem to be needed.

In this scenario, innovative approaches to develop accurate EESM flux-based CCG models are proposed in this article. The primary advantage of the proposed models is to consider stator and rotor windings as two separate but interdependent blocks, as is obtained straightforwardly by means of the VBR formulations, but not with the state-of-the-art CCG models. The article novelties and the benefits of the proposed EESM models are, thus, summarized as follows.

1) The developed EESM models constitute the first CCG formulations with decoupled but interdependent dynamics for the stator and rotor windings, providing enhanced simulation capabilities while preserving ultra-high accuracy. First, the dynamics of the stator winding can be simulated at variable rotor current without requiring the current-to-flux map of the rotor (which is often experimentally unavailable). Second, the rotor winding overvoltage due to sudden stator current variations can be conveniently analyzed by using the stator current as an external input to the rotor block, facilitating the analysis of fault scenarios.
2) Two formulations are presented for accurate modeling of magnetic saturation, including both self- and cross-saturation effects. The two formulations minimize the memory requirements with respect to the existing flux-based models in the literature, by completely avoiding data extrapolation. Moreover, the offline computational

burden of the maps used in the proposed formulations is similar to that of the current-based approach, with drastically reduced computational times.

3) In-depth simulation and experimental comparisons of the proposed and state-of-the-art models are reported, highlighting benefits and drawbacks of each. For this purpose, digital twin tests are performed for the models experimental validation.

In order to substantiate the robustness and validity of the proposed EESM models, the 100 kW sample equipping the Renault Zoe EV R135 has been assumed as a reference case for both the simulation stage and experimental tests.

The rest of this article is organized as follows. Section II introduces the state-of-the-art current-based and flux-based models. In Section III, the proposed EESM CCG models are presented and described in detail. Section IV provides the simulation comparison between proposed and state-of-the-art models, while Section V contains the models experimental validation. Finally, Section VI concludes this article.

II. LITERATURE ANALYSIS OF CCG MODELS

Based on the previously mentioned analysis, the EESM CCG models can be implemented through current-based or flux-based formulations, both considering magnetic saturation by means of maps. These maps are typically expressed in the rotating dq reference frame linked to the machine rotor flux, and are classified as follows.

1) *Current-to-flux* $\boldsymbol{\lambda} = \boldsymbol{\lambda}(\boldsymbol{i})$: The machine currents (stator dq and rotor ones) allow determining the corresponding flux linkages.
2) *Current-to-inductance* $\boldsymbol{l} = \boldsymbol{l}(\boldsymbol{i})$: The machine currents enable the determination of the incremental inductances corresponding to the machine operating point.
3) *Flux-to-current* $\boldsymbol{i} = \boldsymbol{i}(\boldsymbol{\lambda})$: The flux linkages (stator dq and rotor ones) allow determining the corresponding machine currents. These relationships are obtained by numerically inverting the current-to-flux maps. For this reason, in the literature, $\boldsymbol{i} = \boldsymbol{i}(\boldsymbol{\lambda})$ are also referred to as *inverse flux maps*, in contrast to the *direct flux maps* $\boldsymbol{\lambda} = \boldsymbol{\lambda}(\boldsymbol{i})$ [38].

A. CURRENT-BASED MODEL

The dynamic models for EESMs are developed by applying the Park transformation to the stator and rotor voltage equations in phase variables. In this way, the electromagnetic variables are all referred to the dq reference frame, in which the d-axis corresponds to the rotor winding magnetic axis. In Fig. 2, the angle θ_e used for the Park transformation is highlighted for a representative 2-pole machine.

Neglecting the iron losses and the presence of any damper winding on the rotor (normally not used in propulsion and traction applications), the voltage equation of the EESM in the dq reference frame is

$$\boldsymbol{v} = \mathbf{R}\boldsymbol{i} + \frac{d\boldsymbol{\lambda}}{dt} + \omega_e \mathbf{J}\boldsymbol{\lambda} \tag{1}$$

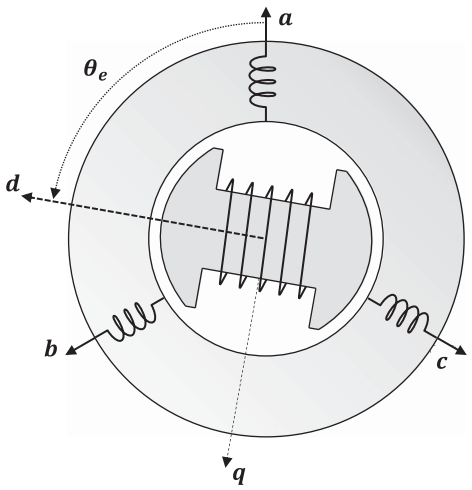


FIGURE 2. Schematic representation of a 2-pole EESM.

where $\boldsymbol{v}$, $\boldsymbol{i}$, and $\boldsymbol{\lambda}$ are the voltage, current, and flux linkage vectors, in the form $\boldsymbol{x} = [x_d;\ x_q;\ x_f]$, whose components are the stator d- and q- and rotor field f-variables. Moreover, ω_e is the electrical pulsation, $\mathbf{R}$ contains the stator R_s and rotor R_f resistances, and $\mathbf{J}$ is the 3×3 matrix used for the calculation of the back-electromotive force

$$\mathbf{R} = \begin{bmatrix} R_s & 0 & 0 \\ 0 & R_s & 0 \\ 0 & 0 & R_f \end{bmatrix}, \quad \mathbf{J} = \begin{bmatrix} 0 & -1 & 0 \\ 1 & 0 & 0 \\ 0 & 0 & 0 \end{bmatrix}. \tag{2}$$

In order to consider iron saturation, the voltage equation is coupled with the nonlinear current-to-flux relationships, defined as in (3) for each flux linkage component

$$\begin{cases} \lambda_d = \lambda_d(i_d, i_q, i_f) \\ \lambda_q = \lambda_q(i_d, i_q, i_f) \\ \lambda_f = \lambda_f(i_d, i_q, i_f). \end{cases} \tag{3}$$

The relationships in (3) determined for the 100 kW EESM under consideration are illustrated in Fig. 3. Using the machine magnetic symmetry, only positive stator q-axis and rotor currents can be considered in the definition of the current-to-flux maps representing the relationships in (3).

In order to develop the current-based dynamic model, the time derivative of the flux linkage vector in (1) is written as follows [50]:

$$\frac{d\boldsymbol{\lambda}(\boldsymbol{i})}{dt} = \boldsymbol{l}(\boldsymbol{i})\frac{d\boldsymbol{i}}{dt} \tag{4}$$

in which $\boldsymbol{l}(\boldsymbol{i})$ is the incremental inductance matrix, whose elements are the flux linkage partial derivatives with respect to the machine currents

$$\boldsymbol{l}(\boldsymbol{i}) = \begin{bmatrix} l_{dd} = \frac{\partial \lambda_d}{\partial i_d} & l_{dq} = \frac{\partial \lambda_d}{\partial i_q} & l_{df} = \frac{\partial \lambda_d}{\partial i_f} \\ l_{qd} = \frac{\partial \lambda_q}{\partial i_d} & l_{qq} = \frac{\partial \lambda_q}{\partial i_q} & l_{qf} = \frac{\partial \lambda_q}{\partial i_f} \\ l_{fd} = \frac{\partial \lambda_f}{\partial i_d} & l_{fq} = \frac{\partial \lambda_f}{\partial i_q} & l_{ff} = \frac{\partial \lambda_f}{\partial i_f} \end{bmatrix}. \tag{5}$$

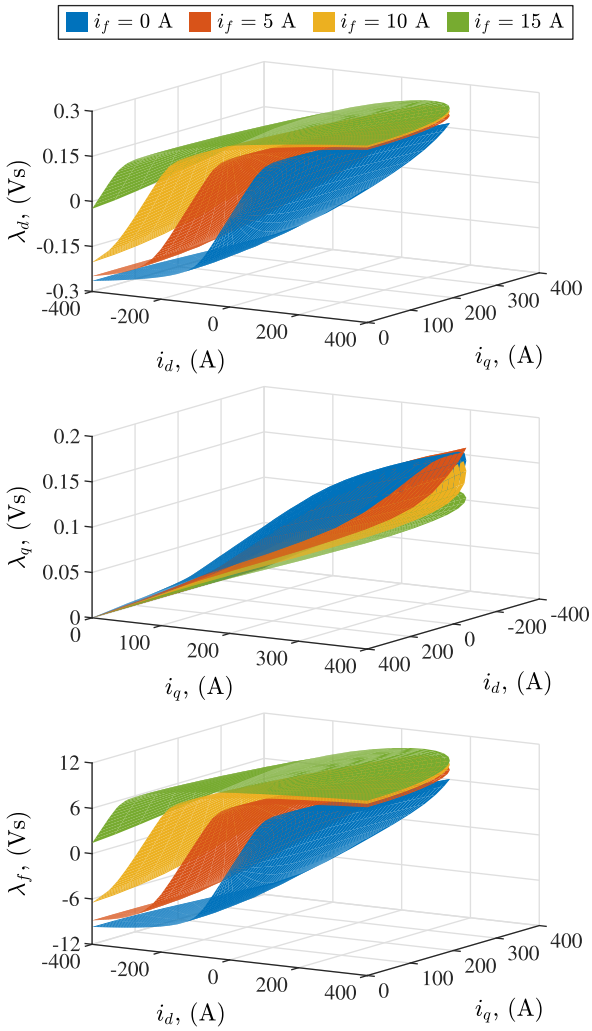


FIGURE 3. Current-to-flux maps of the EESM under consideration.

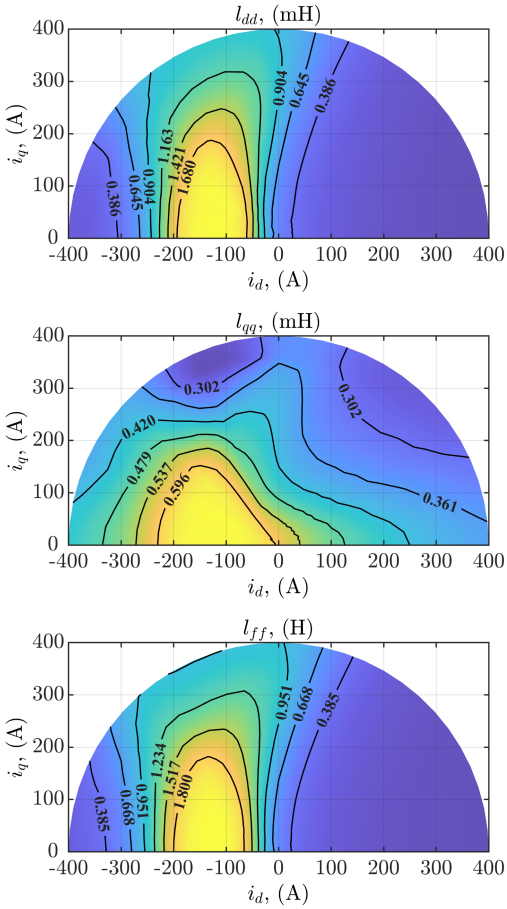


FIGURE 4. Incremental inductances of the EESM under consideration for i_f equal to 5 A.

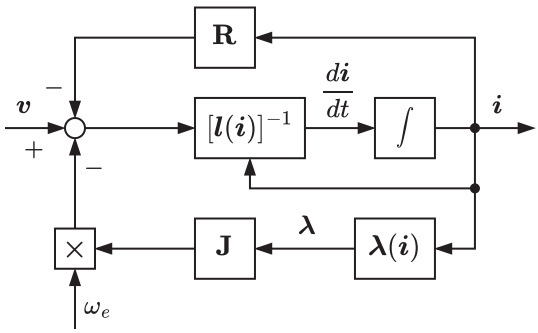


FIGURE 5. EESM current-based CCG model [50].

The representative values of l_{dd}, l_{qq}, and l_{ff} at an arbitrary rotor current are presented in Fig. 4. It can be noted that the rotor self-incremental inductance is orders of magnitude larger than the stator ones.

By replacing the flux derivatives from (4) into the voltage equation (1), the time derivatives of the currents constituting the EESM current-based model are obtained, along with the schematic representation in Fig. 5

$$\frac{d\boldsymbol{i}}{dt} = [\boldsymbol{l}(\boldsymbol{i})]^{-1}[\boldsymbol{v} - \mathbf{R}\boldsymbol{i} - \omega_e \mathbf{J}\boldsymbol{\lambda}(\boldsymbol{i})]. \tag{6}$$

The values of the incremental inductance matrix elements are retrieved by interpolating the current-to-inductance maps. At each simulation time step, $\boldsymbol{l}(\boldsymbol{i})$ is also inverted to compute the time derivatives of the state-space variables by means of (6). The numerical accuracy and computational effort of the model can be improved by determining $[\boldsymbol{l}(\boldsymbol{i})]^{-1}$ offline, i.e., prior to the simulation. In this regard, the machine currents are used to retrieve the inverse matrix elements directly, thus avoiding the online inversion of $\boldsymbol{l}(\boldsymbol{i})$.

The current-based approach preserves its straightforward implementation regardless of the methodology adopted for computing $[\boldsymbol{l}(\boldsymbol{i})]^{-1}$. Nevertheless, convergence issues may appear in case of significant magnetic saturation, since the numerical gradients of the flux linkages directly establish the time derivatives of the currents [47], [53], [54].

B. FLUX-BASED MODEL

The state-of-the-art flux-based CCG model reported in the literature will hereinafter be referred to as the *single-step*

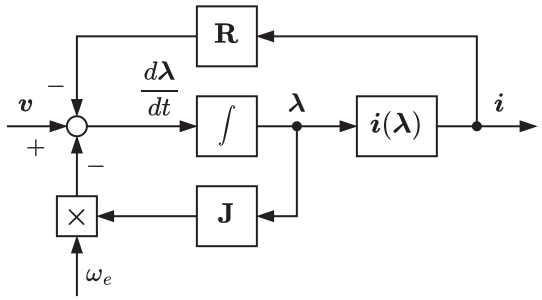


FIGURE 6. EESM single-step flux-based CCG model with flux-to-current maps [52].

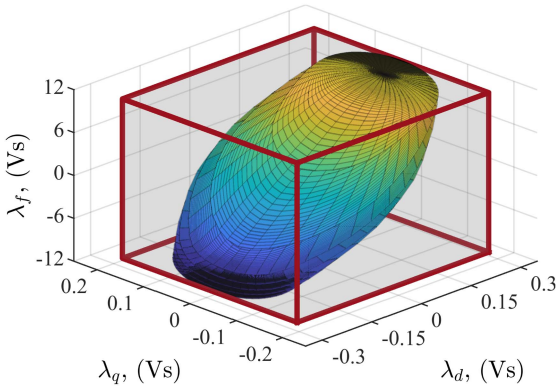


FIGURE 7. Flux linkages and the smallest external cuboid domain.

model, to distinguish it from the models with decoupled stator and rotor dynamics proposed in this article. Indeed, the term single-step is used to indicate that both the stator and rotor currents are simultaneously obtained by interpolating the flux-to-current maps. The implementation of the single-step model is more complex and time-consuming compared to the current-based alternative, due to the iterative procedure needed for the flux-to-current maps determination.

Starting from (1), the EESM single-step flux-based model, which is schematically shown in Fig. 6, is formulated as

$$\frac{d\boldsymbol{\lambda}}{dt} = \boldsymbol{v} - \mathbf{R}\boldsymbol{i} - \omega_e \mathbf{J}\boldsymbol{\lambda} \tag{7}$$

$$\boldsymbol{i} = \boldsymbol{i}(\boldsymbol{\lambda}). \tag{8}$$

At each time instant of the simulation, the flux linkages allow determining the machine currents by means of the flux-to-current relationships (8). In the single-step model, the flux linkage vector is the input of three different maps, whose computation and interpolation are nontrivial [51].

In addition, the definition of the flux domain for these maps is not unique. The most direct choice for the flux linkage domain of (8) corresponds to the smallest cuboid enclosing all the fluxes combinations from the current-to-flux maps, as depicted in Fig. 7. By defining equally spaced flux values inside the cuboid, the corresponding machine currents are determined to obtain the output of the relationships in (8).

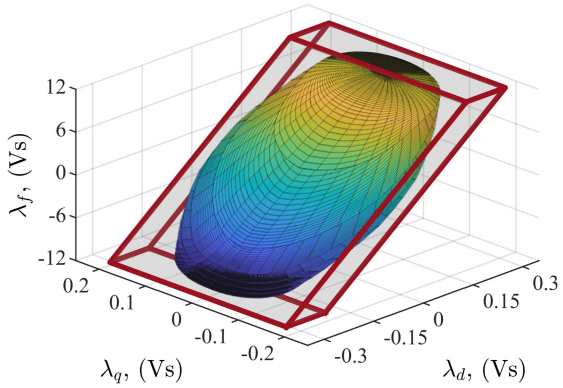


FIGURE 8. Improved domain selection for the flux-to-current maps.

However, many points included in the cuboid are obtained by data extrapolation, since they do not belong to the current-to-flux maps. Moreover, the fine discretization required for the useful domain applies also to the extrapolated fluxes, leading to significant computational efforts. An alternative domain selection is represented by the largest cuboid entirely enclosed by the flux linkages. Nevertheless, many useful flux linkages combinations would be excluded from the flux-to-current maps determination.

The approach developed in [52] allows solving the issue of the domain selection. For this purpose, the flux linkages are defined in a new reference system by means of (9), being $\mathbf{G}_{\boldsymbol{\lambda}}$ the transformation matrix and $\boldsymbol{\lambda}_G$ the obtained flux vector

$$\boldsymbol{\lambda}_G = \mathbf{G}_{\boldsymbol{\lambda}}\boldsymbol{\lambda}. \tag{9}$$

In the transformed coordinate system, a prism capable of tightly enclosing the fluxes combinations can be determined, as shown in Fig. 8, leading to several advantages compared to the other possible domains. Indeed, the extrapolated points for the flux-to-current maps are strongly reduced, while all the fluxes are considered with good discretization inside the useful domain. The resulting flux-to-current relationships for the single-step model are therefore defined as follows:

$$\begin{cases} i_d = i_d(\lambda_{dG}, \lambda_{qG}, \lambda_{fG}) \\ i_q = i_q(\lambda_{dG}, \lambda_{qG}, \lambda_{fG}) \\ i_f = i_f(\lambda_{dG}, \lambda_{qG}, \lambda_{fG}) \end{cases} \tag{10}$$

through which the machine currents are determined using the transformed flux vector components. The corresponding simulation block diagram is provided in Fig. 9.

The $\mathbf{G}_{\boldsymbol{\lambda}}$ needed in the model implementation is computed using the current-to-flux relationships [52]. For this purpose, the covariance matrix $\mathbf{cov}_{\boldsymbol{\lambda}}$ of all the fluxes combinations is first determined. Subsequently, the diagonal matrix $\mathbf{G}_{\mathbf{S}}$ with the corresponding eigenvalues and the full matrix $\mathbf{G}_{\mathbf{R}}$ with the eigenvectors are also determined according to (11)

$$\mathbf{cov}_{\boldsymbol{\lambda}}\mathbf{G}_{\mathbf{R}} = \mathbf{G}_{\mathbf{R}}\mathbf{G}_{\mathbf{S}}. \tag{11}$$

A possible formulation for $\mathbf{G}_{\boldsymbol{\lambda}}$ consists of (12), in which $\mathbf{G}_{\mathbf{R}}$ is related to a domain rotation, whereas $\mathbf{G}_{\mathbf{S}}$ corresponds

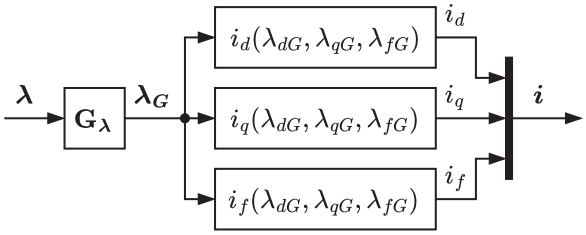


FIGURE 9. Currents determination in the single-step flux-based model [52].

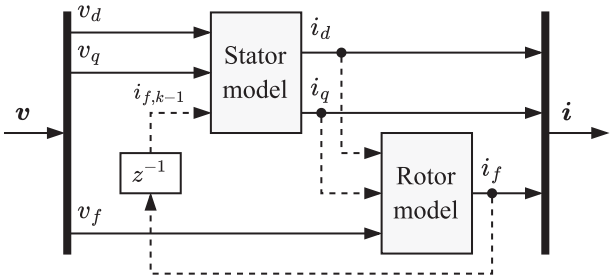


FIGURE 10. EESM model with decoupled dynamics.

to a scaling of variables

$$\mathbf{G}_{\boldsymbol{\lambda}} = \left(\mathbf{G}_{\mathbf{R}}\sqrt{\mathbf{G}_{\mathbf{S}}}\right)^{-1}. \tag{12}$$

Finally, the single-step flux-based model is completed with the output currents of the flux-to-current maps. In this regard, systematic evaluations of current vectors are performed until the corresponding fluxes match the reference ones within a prescribed tolerance. An iterative search is, thus, performed from a starting point toward the objective fluxes minimizing error functions, for every point in the flux-to-current maps.

The single-step model with the improved domain selection represents a straightforward solution for the EESM dynamic modeling. Nevertheless, computing the flux-to-current maps remains a time-consuming procedure, as an iterative search needs to be performed. An interesting alternative to the method proposed in [52] is represented by the data-driven approaches, which are well suited for EESM CCG modeling based on flux-to-current maps, to approximate the nonlinear relationships between flux linkages and currents [55].

III. PROPOSED EESM CCG MODELS

The proposed EESM CCG modeling formulations belong to the flux-based category. In this regard, the stator and the rotor flux linkage dynamics are simulated by means of two distinct systems, interacting through the corresponding currents. As it can be observed in Fig. 10, the rotor current is an input of the stator model, while the stator current components constitute inputs of the rotor block.

The presence of separate stator and rotor blocks introduces a twofold benefit. First, independent numerical simulations of the stator winding can be performed for variable i_f values, as λ_f does not constitute an input of the stator block. This enables partial machine analyses when the rotor current-to-flux relationship is not determined, differently from the state-of-the-art EESM models, which necessarily require the rotor map.

Second, the effects of stator current transients on the flux linkage and voltage of the field winding can be conveniently evaluated with high accuracy by directly imposing both the i_d and i_q profiles to the input of the rotor block. This feature is particularly useful for the analysis of rotor overvoltages caused by stator winding openings, following inverter faults or overcurrent protection.

In the decoupled-dynamics EESM model, the rotor current of the previous time instant $i_{f,k-1}$ must be used to compute the stator current components and is retrieved by means of a delay z^{-1} block. This necessarily introduces also an initial condition for i_f, for the solution of the first simulation step. Nevertheless, the loss of accuracy is negligible when using $i_{f,k-1}$, considering the small time step commonly adopted by the numerical solvers.

The complete block diagram of the proposed EESM CCG models is shown in Fig. 11. The input stator voltages are transformed into the corresponding dq variables by means of the Park transformation, for which the mechanical rotor position θ_m is also needed. The rotational speed ω_m from the mechanical model is another input and allows retrieving the electrical speed. The CCG model returns the currents for the current-controlled generators and the electromagnetic torque T_e for the mechanical model.

In order to obtain accurate simulation results with regard to the nonlinearities of magnetic saturation, two approaches are possible for the proposed decoupled-dynamics EESM models. The first approach relies on flux-to-current maps, while the second involves the so-called *flux-error* maps. In the following, the two alternative approaches are presented.

A. FLUX-TO-CURRENT MAPS APPROACH

According to the schematic representation reported in Fig. 10 for the decoupled-dynamics EESM model, the separation of the stator and rotor voltage equations constitutes a convenient choice for the implementation of the proposed models.

1) STATOR MODEL WITH FLUX-TO-CURRENT MAPS

Neglecting the iron losses, the stator voltage equation in the dq reference frame is

$$\boldsymbol{v}_s = R_s\boldsymbol{i}_s + \frac{d\boldsymbol{\lambda}_s}{dt} + \omega_e\mathbf{J}_\mathbf{s}\boldsymbol{\lambda}_s \tag{13}$$

in which $\boldsymbol{v}_s$, $\boldsymbol{i}_s$, and $\boldsymbol{\lambda}_s$ are the stator voltage, current, and flux linkage vectors, in the form $\boldsymbol{x}_s = [x_d;\ x_q]$, whereas $\mathbf{J}_\mathbf{s}$ is the 2×2 matrix related to the stator back-electromotive force, being $\mathbf{J}_\mathbf{s} = [0, -1;\ 1, 0]$. Starting from (13), the time derivative of the stator flux linkages can be expressed as

$$\frac{d\boldsymbol{\lambda}_s}{dt} = \boldsymbol{v}_s - R_s\boldsymbol{i}_s - \omega_e\mathbf{J}_\mathbf{s}\boldsymbol{\lambda}_s \tag{14}$$

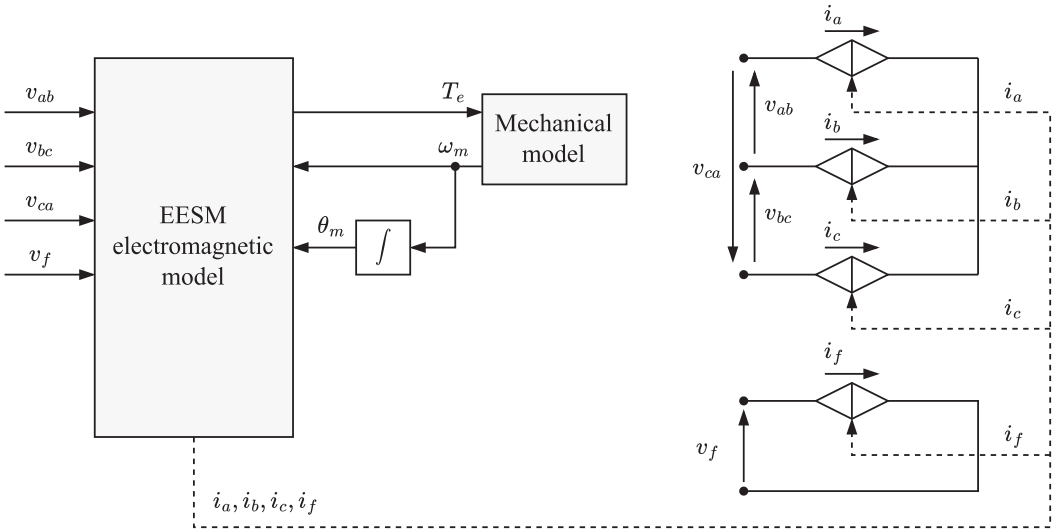


FIGURE 11. Proposed current-controlled generators model for EESMs.

which needs to be associated with flux-to-current maps to determine the stator current vector. Within this context, the stator flux-to-current relationships in the EESM model with decoupled dynamics can be defined as

$$\begin{cases} i_d = i_d(\lambda_{d,pu}, \lambda_{q,pu}, i_f) \\ i_q = i_q(\lambda_{d,pu}, \lambda_{q,pu}, i_f). \end{cases} \tag{15}$$

The motivation behind the introduction of the normalized flux linkage components in (15) is the variable rotor current. Indeed, the flux boundaries of the stator current-to-flux maps change depending on the i_f, and the interpolation domain of the corresponding flux-to-current maps needs to be regulated accordingly. The normalization procedure allows limiting the interpolation domain between constant boundary values, thus enabling the definition of a single fluxes grid for all the rotor currents. In order to determine the stator flux-to-current maps with the normalized domain, two rounds of interpolation are required for each i_f in the current-to-flux maps [53], [56].

The first interpolation involves the stator flux linkages of the current-to-flux maps, which are reported in Fig. 12(a) for an arbitrary rotor current. Inside the considered domain, new flux linkages combinations are defined to generate a regular grid, thus enabling the systematic boundaries determination for every i_f value, as represented in Fig. 12(b). In particular, both the minimum and the maximum d-axis fluxes, $\lambda_{d,\min}$ and $\lambda_{d,\max}$, respectively, depend solely on the rotor current, while the maximum q-axis flux $\lambda_{q,\max}$ depends also on λ_d. The minimum λ_q is constantly zero and the operation with negative i_q is considered through the magnetic symmetry.

The determination of the flux linkage boundaries is needed for the domain normalization, as reported in Fig. 12(c). In order to obtain the flux linkages grid valid for all the rotor currents as required by (15), a second interpolation of the flux linkage components is performed, leading to the domain

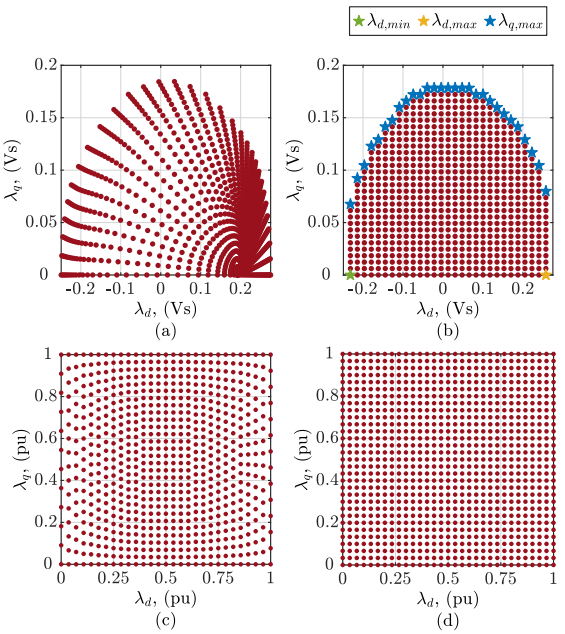


FIGURE 12. Elaboration of the stator flux-to-current maps domain for the EESM under consideration. (a) Stator flux linkages for i_f equal to 5 A. (b) Boundaries determination. (c) Normalized domain. (d) Final flux domain.

in Fig. 12(d). Similarly, the i_d and i_q constituting the output of the flux-to-current maps are obtained by interpolating the values in the current-to-flux relationships, first for the fluxes domain in Fig. 12(b), and second for the values in Fig. 12(d). The simulation block diagram is shown in Fig. 13, where the use of $i_{f,k-1}$ discussed previously can be noted, also for the normalization block.

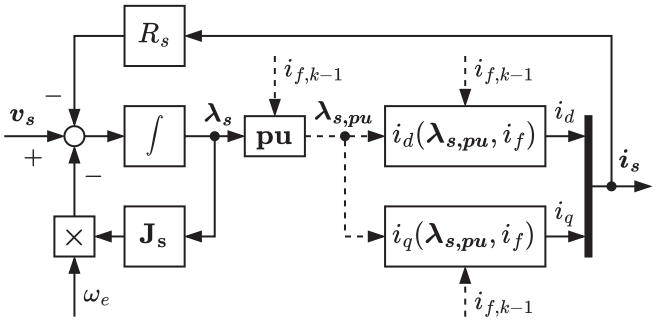


FIGURE 13. Stator model with flux-to-current maps [53].

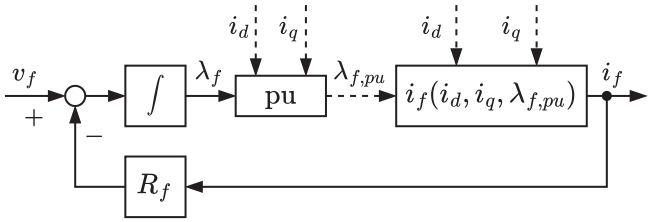


FIGURE 14. Rotor model with flux-to-current map.

The domain elaboration for the stator maps in the model with decoupled dynamics prevents any artificial extrapolation of data outside the boundary of the maps, differently from the methodology of the state-of-the-art flux-based CCG model. Therefore, the proposed EESM model features minimized memory requirements and optimal discretization of the flux-to-current maps. Furthermore, since the output currents of the maps are not computed by means of iterative procedures but rather through interpolation, the computational burden is close to that of the state-of-the-art current-based model.

The stator model can be completed with the expression in (16) for the electromagnetic torque, valid also for the state-of-the-art models

$$T_e = \frac{3}{2} p \left(\boldsymbol{\lambda_s} \wedge \boldsymbol{i_s}\right) = \frac{3}{2} p \left(\lambda_d i_q - \lambda_q i_d\right) \tag{16}$$

where p is the number of pole pairs.

2) ROTOR MODEL WITH FLUX-TO-CURRENT MAP

The rotor voltage equation consists of

$$v_f = R_f i_f + \frac{d\lambda_f}{dt} \tag{17}$$

from which the time derivative of the flux linkage can be computed as

$$\frac{d\lambda_f}{dt} = v_f - R_f i_f. \tag{18}$$

Similarly to the stator model, the flux derivative in (18) is associated with a flux-to-current map for the determination of the rotor current, in the form

$$i_f = i_f(i_d, i_q, \lambda_{f,pu}). \tag{19}$$

The determination of the rotor flux-to-current relationship represents a less demanding task compared to the stator case, as the 2-D normalization procedure is not required. Indeed, for every combination of stator current vector components, the one-to-one relationship between i_f and λ_f is considered. The minimum and maximum rotor flux linkages are used to normalize λ_f, thus obtaining the $\lambda_{f,pu}$ values corresponding to i_f. By means of interpolations, the output currents of (19) are determined for the domain of normalized flux linkages, valid for every i_d and i_q combination. The rotor model with flux-to-current map for the decoupled-dynamics approach is provided in Fig. 14.

The rotor flux-to-current relationship includes only useful points and the considerations formulated for the stator maps remain valid also for (19). In this regard, the CCG model with decoupled dynamics represents the unique possibility of implementing a flux-based model without data extrapolation, while exhibiting also reduced offline computational burden.

B. FLUX-ERROR MAPS APPROACHES

The proposed decoupled-dynamics EESM model can also be implemented by means of flux-error maps for both the stator and rotor blocks. In this case, the model simulation capabilities are the same as those of the flux-to-current maps approach, since the EESM model structure in Fig. 10 is not modified. In this article, the flux-error maps represent the flux deviations between the outputs of current-to-flux maps and fluxes of an arbitrary model assumed as a reference. The inputs of the maps can consist of currents or flux linkages.

According to the literature, the flux-error maps constitute an alternative methodology to consider magnetic saturation nonlinearities in dynamic models, with respect to the flux-to-current maps [57], [58]. The concept of flux-errors has been first introduced in [57] for the asynchronous machines, and recently adopted in [58] to implement a modular dynamic model for multi-three-phase EESMs. Furthermore, a similar approach in which unsaturated reactances are modified by multiplication factors to consider magnetic saturation can be also implemented, as presented in [59]. In the following, two possible stator models with flux-error maps are proposed.

1) STATOR MODEL WITH FLUX-ERROR MAPS: APPROACH A

Regarding the time derivative of the stator flux linkage, the following expression can be introduced for the relationship between $\boldsymbol{\lambda_s}$ and $\boldsymbol{i_s}$

$$\boldsymbol{\lambda_s} = L_{\sigma s} \boldsymbol{i_s} + \boldsymbol{\lambda_{mag}} \tag{20}$$

in which $L_{\sigma s}$ and $\boldsymbol{\lambda_{mag}}$ are the stator leakage inductance and the stator magnetizing flux linkage, respectively. The $\boldsymbol{i_s}$ resulting from (20) can be replaced into (14), thus leading to the time derivative (21) for $\boldsymbol{\lambda_s}$ in the EESM CCG model with flux-error maps

$$\frac{d\boldsymbol{\lambda_s}}{dt} = \boldsymbol{v_s} + \frac{R_s}{L_{\sigma s}} \boldsymbol{\lambda_{mag}} - \frac{R_s}{L_{\sigma s}} \boldsymbol{\lambda_s} - \omega_e \mathbf{J_s} \boldsymbol{\lambda_s}. \tag{21}$$

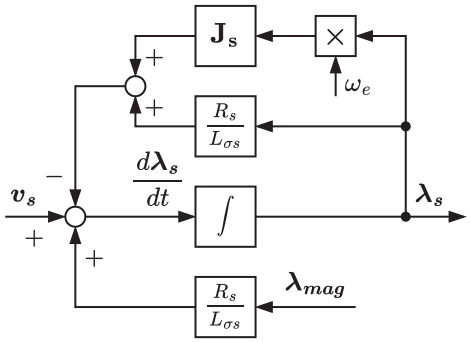


FIGURE 15. Stator model for the approach with flux-error maps.

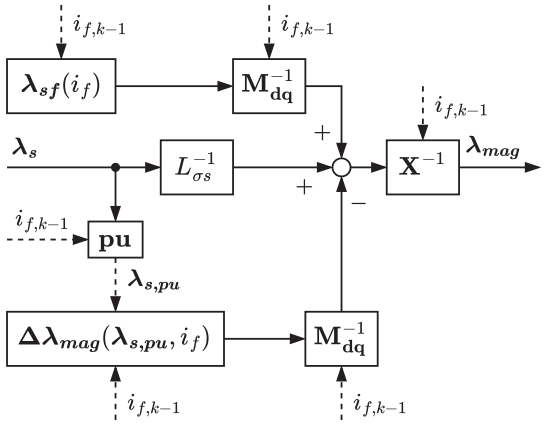


FIGURE 16. Computation of the stator magnetizing flux linkage.

The corresponding block diagram is reported in Fig. 15. Although $L_{\sigma s}$ is introduced in the proposed stator model, the accurate estimation of this parameter is not required. In fact, an arbitrary value can be chosen and the resulting flux-error maps will change accordingly, even though nonsmooth flux-error maps may be obtained.

In order to include the nonlinearities due to iron saturation, the stator reference model must be defined, along with the corresponding flux-error maps. For this purpose, the d- and q- components of $\boldsymbol{\lambda_{mag}}$ are computed as in (22) by means of the current-to-flux maps and leakage inductance

$$\begin{cases} \lambda_{mag,d}(i_d, i_q, i_f) = \lambda_d(i_d, i_q, i_f) - L_{\sigma s} i_d \\ \lambda_{mag,q}(i_d, i_q, i_f) = \lambda_q(i_d, i_q, i_f) - L_{\sigma s} i_q. \end{cases} \tag{22}$$

Starting from (22), the stator magnetizing flux linkage $\boldsymbol{\lambda_{sf}}$ in open-circuit, generated solely by the field winding, can be determined as

$$\boldsymbol{\lambda_{sf}} = \begin{bmatrix} \lambda_{mag,d}(0, 0, i_f) \\ 0 \end{bmatrix}. \tag{23}$$

In addition, the magnetizing inductances of the arbitrary reference model are computed as

$$\begin{cases} M_d = \frac{\lambda_{mag,d}(i_d, 0, i_f) - \lambda_{sf,d}}{i_d} \\ M_q = \frac{\lambda_{mag,q}(0, i_q, i_f)}{i_q}. \end{cases} \tag{24}$$

Therefore, the magnetizing flux linkage can be written as

$$\boldsymbol{\lambda_{mag}} = \boldsymbol{\lambda_{sf}} + \mathbf{M_{dq}} \boldsymbol{i_s} - \boldsymbol{\Delta\lambda_{mag}} \tag{25}$$

in which $\mathbf{M_{dq}} = [M_d, 0;\ 0, M_q]$. In (25), $\boldsymbol{\lambda_{sf}} + \mathbf{M_{dq}} \boldsymbol{i_s}$ constitutes the stator reference model, while $\boldsymbol{\Delta\lambda_{mag}}$ are the corresponding flux linkage deviations represented by the flux-error maps.

Finally, the current expression from (20) can be substituted in (25), leading to the formulation adopted in the simulation environment

$$\boldsymbol{\lambda_{mag}} = \mathbf{X}^{-1} \left(\mathbf{M_{dq}^{-1}} \boldsymbol{\lambda_{sf}} + \frac{\boldsymbol{\lambda_s}}{L_{\sigma s}} - \mathbf{M_{dq}^{-1}} \boldsymbol{\Delta\lambda_{mag}} \right) \tag{26}$$

in which $\mathbf{X} = \mathbf{M_{dq}^{-1}} + L_{\sigma s}^{-1} \mathbb{I}_{2\times 2}$ for clarity reasons, being $\mathbb{I}_{2\times 2}$ the identity matrix. The block diagram adopted for the $\boldsymbol{\lambda_{mag}}$ computation is provided in Fig. 16, in which the use of the rotor current from the previous time step can be noted.

Similarly to the flux-to-current maps (15) in the alternative modeling approach, the stator flux-error maps are defined as in (27), functions of the normalized flux linkage components and of the rotor current

$$\begin{cases} \Delta\lambda_{mag,d} = \Delta\lambda_{mag,d}(\lambda_{d,pu}, \lambda_{q,pu}, i_f) \\ \Delta\lambda_{mag,q} = \Delta\lambda_{mag,q}(\lambda_{d,pu}, \lambda_{q,pu}, i_f). \end{cases} \tag{27}$$

The normalized flux linkage components are necessary to take into account the effects of the variable rotor current on the boundary of the maps, as discussed previously for the flux-to-current relationships.

In this regard, the same normalization procedure described in Fig. 12 is adopted to determine the stator flux-error maps in (27). The d- and q- flux-errors $\Delta\lambda_{mag,d}$ and $\Delta\lambda_{mag,q}$ are computed by means of (25) for the currents in the current-to-flux relationships. The flux-errors are therefore referred to a single fluxes grid valid for all the considered i_f values, thus obtaining (27) through the normalization procedure.

It must be noticed that the definition of the stator reference model in (25) has a significant impact on the resulting flux-error maps. Indeed, different formulations can be used for the reference model and the corresponding flux-error maps will adapt accordingly. Nevertheless, the unsaturated condition constitutes the most convenient choice, particularly for the $\mathbf{M_{dq}}$ computation, since it minimizes the interpolation issues at the boundary of the flux-error maps. Besides, the choice of a particular combination of stator current components allows having $\mathbf{M_{dq}}$ as a function of the i_f only, as shown in Fig. 16.

The d- and q- flux-error maps corresponding to a stator reference model determined in the unsaturated condition are represented in Fig. 17 for an arbitrary positive rotor current. In order to provide a straightforward explanation of the flux-error maps behavior, the flux linkage domain in Fig. 12(b) has been adopted.

As it can be seen in Fig. 17, the d-axis flux-error is close to zero for low λ_d. In these conditions, the d-axis exhibits limited saturation and the reference model provides a good

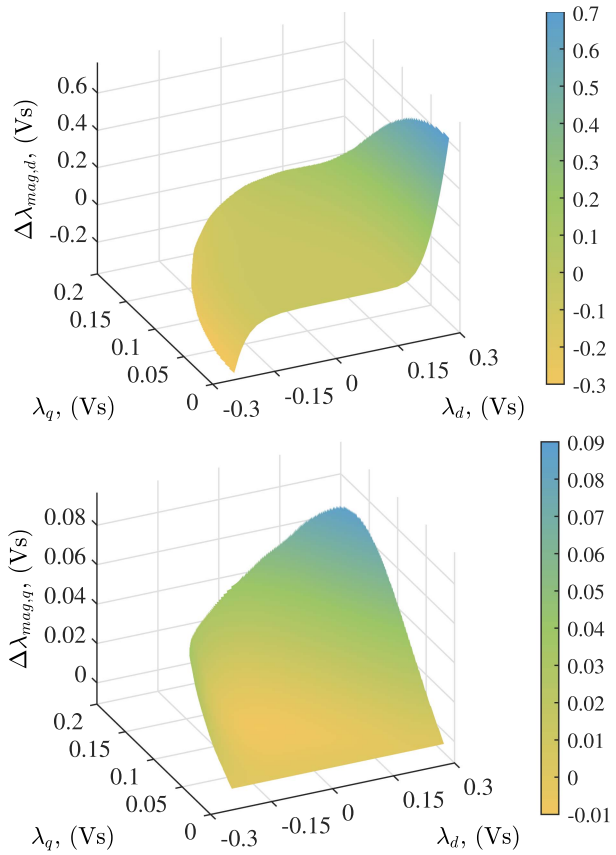


FIGURE 17. Stator flux-error maps of the EESM under consideration for i_f equal to 5 A.

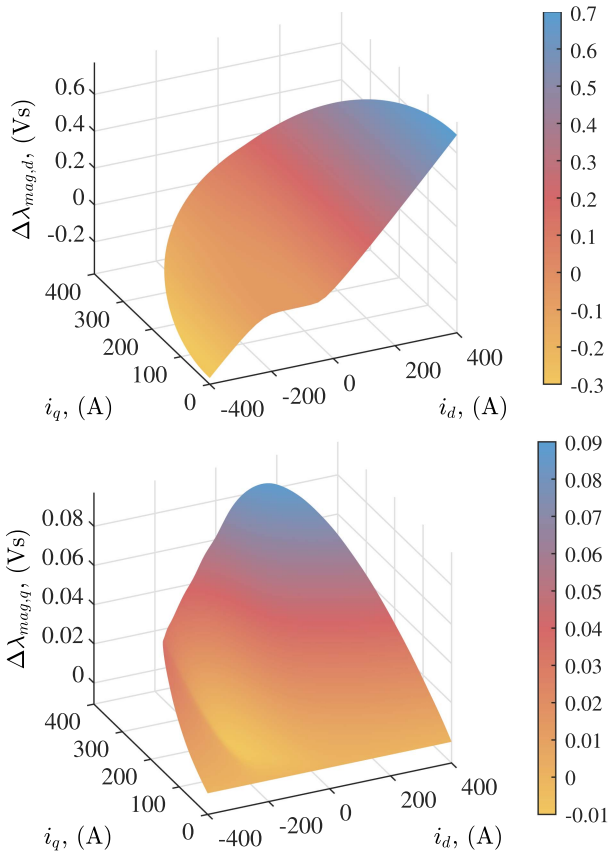


FIGURE 18. Stator flux-error maps with current domain of the EESM under consideration for i_f equal to 5 A.

estimation of the flux. Conversely, for increasing λ_d values, the flux-error becomes progressively larger, to compensate for the deviations of the reference model with respect to the $\lambda_{mag,d}$ in (22). In addition, the impact of cross-saturation can be observed, as $\Delta\lambda_{mag,d}$ rises together with the value of λ_q, when λ_d is fixed. Similar observations can be formulated also for the q-axis flux-error. The operation with negative i_q is considered by means of the machine magnetic symmetry.

Regarding the computation of the electromagnetic torque, the current vector determined through (20) can be replaced in (16), leading to an equivalent expression specific for the flux-error maps approach

$$T_e = \frac{3}{2} p \left(\frac{\boldsymbol{\lambda_{mag}} \wedge \boldsymbol{\lambda_s}}{L_{\sigma s}} \right). \tag{28}$$

Since the normalization procedure is adopted for the stator modeling with flux-error maps, this alternative approach for the EESM modeling with decoupled dynamics prevents any artificial extrapolation of data outside the boundary of the maps, similarly to the flux-to-current maps formulation. Moreover, reduced offline computational burden is required also for this implementation, as conventional interpolation methods are used to determine the flux-error maps.

2) STATOR MODEL WITH FLUX-ERROR MAPS: APPROACH B

The implementation of the stator model can be simplified by expressing the d- and q- flux-error relationships as functions of the stator and rotor currents, in the form

$$\begin{cases} \Delta\lambda_{mag,d} = \Delta\lambda_{mag,d}(i_d, i_q, i_f) \\ \Delta\lambda_{mag,q} = \Delta\lambda_{mag,q}(i_d, i_q, i_f). \end{cases} \tag{29}$$

The determination of (29) consists in computing the flux-errors by means of (25) for regularly spaced currents, without performing the domain elaboration reported in Fig. 12, thus preventing the interpolation of scattered values. The resulting flux-error maps with current domain are presented in Fig. 18 for an arbitrary positive rotor current and the considerations formulated on the behavior of (27) remain also valid.

The adoption of the current domain constitutes the fastest method to implement the stator model in the CCG modeling approach with decoupled dynamics, since no interpolation of scattered data is required. Nevertheless, the solution of the stator model requires delay blocks for i_d and i_q, which are needed at the beginning of the simulation step to determine $\boldsymbol{\Delta\lambda_{mag}}$, and whose effect is typically negligible due to the small time step of the numerical solvers. The block diagram for the $\boldsymbol{\lambda_{mag}}$ computation by means of flux-error maps with current domain is provided in Fig. 19.

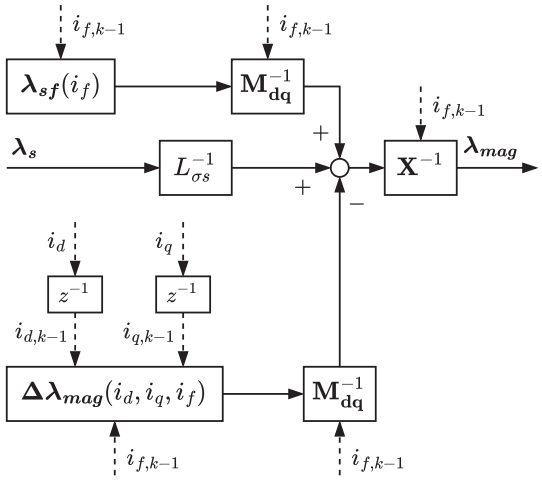


FIGURE 19. Computation of the stator magnetizing flux linkage by means of flux-error maps with current domain.

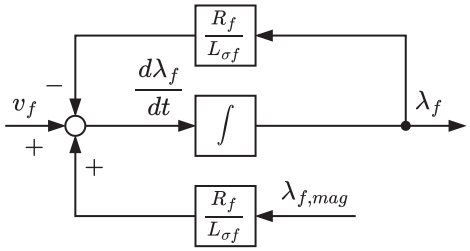


FIGURE 20. Rotor model for the approach with flux-error map [58].

3) ROTOR MODEL WITH FLUX-ERROR MAP

In order to implement the rotor model in Fig. 10 using the flux-error maps approach, the flux linkage can be written as

$$\lambda_f = L_{\sigma f} i_f + \lambda_{f,mag} \tag{30}$$

where $L_{\sigma f}$ and $\lambda_{f,mag}$ are the rotor leakage inductance and the rotor magnetizing flux linkage, respectively. The resulting i_f can be replaced into (18), thus leading to the time derivative in (31) and to the block diagram in Fig. 20

$$\frac{d\lambda_f}{dt} = v_f + \frac{R_f}{L_{\sigma f}}\lambda_{f,mag} - \frac{R_f}{L_{\sigma f}}\lambda_f. \tag{31}$$

Similarly to the stator model, an arbitrary value of $L_{\sigma f}$ can be chosen and the flux-error map will change accordingly.

As in the stator case, a rotor reference model is defined, along with the corresponding flux-error map, to consider the effects of magnetic saturation. For this purpose, $\lambda_{f,mag}$ can be computed as

$$\lambda_{f,mag} = \lambda_f(i_d, i_q, i_f) - L_{\sigma f} i_f. \tag{32}$$

Starting from (32), the rotor magnetizing flux linkage λ_{fs} generated solely by the stator winding can be determined as

$$\lambda_{fs} = \lambda_{f,mag}(i_d, i_q, 0) \tag{33}$$

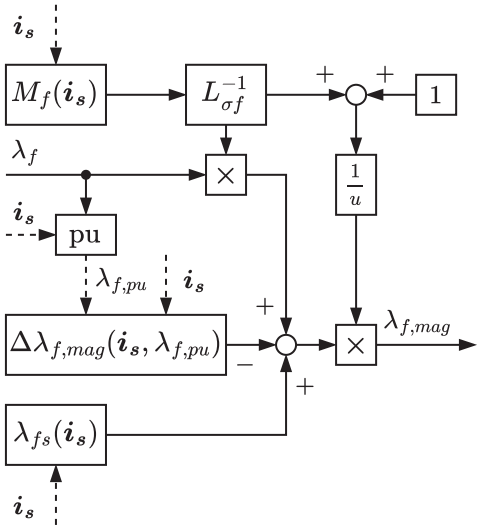


FIGURE 21. Computation of the rotor magnetizing flux linkage.

whereas the rotor magnetizing inductance M_f is computed by means of (34)

$$M_f = \frac{\lambda_{f,mag}(i_d, i_q, i_f) - \lambda_{fs}}{i_f}. \tag{34}$$

Finally, the rotor magnetizing flux linkage is expressed as

$$\lambda_{f,mag} = \lambda_{fs} + M_f i_f - \Delta\lambda_{f,mag} \tag{35}$$

where $\lambda_{fs} + M_f i_f$ constitutes the rotor reference model, while $\Delta\lambda_{f,mag}$ is the corresponding flux-error map. In this context, the rotor flux-error map allows compensating for the deviations between the reference model and $\lambda_{f,mag}$ in (32).

The formulation for $\lambda_{f,mag}$ in the simulation environment is obtained by replacing in (35) the rotor current expression derived from (30), leading to (36) and to the block diagram shown in Fig. 21

$$\lambda_{f,mag} = \frac{1}{M_f L_{\sigma f}^{-1} + 1}\left(\lambda_{fs} + \frac{M_f}{L_{\sigma f}}\lambda_f - \Delta\lambda_{f,mag}\right). \tag{36}$$

Analogously to the stator model, the choice of a particular rotor current allows having M_f as a function of the $\boldsymbol{i_s}$ only, as represented in Fig. 21.

For the rotor modeling, the determination of the flux-error map as a function of the rotor flux linkage can be achieved as in (37), through the flux-error relationship which is obtained from (35) and which is a function of currents only

$$\Delta\lambda_{f,mag} = \Delta\lambda_{f,mag}(i_d, i_q, \lambda_{f,pu}). \tag{37}$$

The same normalization procedure used for (19) permits replacing the i_f values in the domain with $\lambda_{f,pu}$ elements. In this way, only useful points are included in the normalized domain of (37), thus proving that the flux-error formulation represents a complete alternative to the proposed CCG model based on flux-to-current maps.

TABLE 1. Main Specifications of the EESM Under Test

Peak power	100 kW
Peak torque	245 N·m
Number of poles	4
Rated DC-link voltage	350 V
Maximum peak stator current $I_{s,\max}$	400 A
Maximum rotor current $I_{f,\max}$	15 A

Similarly to the stator model, the rotor flux-error map can also be implemented in terms of currents only, as explored in [58]. However, the advantages related to the rotor model implementation are not significant, since the interpolation of scattered values involves exclusively the 1-D relationship between i_f and λ_f at fixed stator current components.

IV. SIMULATION RESULTS

The proposed EESM models with decoupled stator and rotor dynamics have been implemented in simulation environment, before proceeding with the experimental validation tests. The software consists of MATLAB/Simulink, for both the offline generation of the multidimensional maps and the preliminary analyses of the correctness of the models. Furthermore, the state-of-the-art current-based and flux-based models have also been implemented for comparison purposes. For the current-based model, $[\boldsymbol{l}(\boldsymbol{i})]^{-1}$ has been determined offline to reduce the computational burden, as discussed in Section II. Regarding the single-step flux-based model proposed in the literature, the matrix in (12) for the new reference system has been used, although other formulations can be adopted.

All the models have been implemented using the data of an EESM sample from the Renault Zoe EV R135, for which the main specifications are reported in Table 1. In addition, the current-to-flux maps, which are presented in Fig. 3, have been obtained experimentally by means of the identification procedures described in the literature [60], [61].

A. OFFLINE MAPS GENERATION

In order to implement the EESM models and compare the computation times required for the maps, a discretization of 151 points has been chosen in each dimension, regardless of the considered model. Furthermore, the models have been derived for positive i_q and i_f only, since the corresponding negative values can be included using the machine magnetic symmetry. All the CCG models have been implemented and run on a PC featuring Windows 11 as the operating system, equipped with an Intel Xeon w7-2495X (2.50 GHz, 24 cores) processor and 256 GB of RAM.

As it can be noted in Table 2, all the EESM CCG models, except for the single-step flux-based one, require less than one minute to be derived offline. The implementation based on the flux-error maps with current domain constitutes the fastest approach, since the normalization procedure repeated for all the rotor currents is completely avoided. The current-based model is the second fastest, involving the computation of

TABLE 2. Offline Computation Times for the Maps Generation

Model	Stator	Rotor	Total time
Current-based	N/A	N/A	13.4 s
Single-step flux-based	N/A	N/A	1 h 15 min
Proposed model with flux-to-current maps, in Section III-A	33.9 s	2.6 s	36.5 s
Proposed model with flux-error maps, in Section III-B1	50.9 s	1.4 s	52.3 s
Proposed model with flux-error maps (current domain), in Section III-B2	4.2 s	1.5 s	5.7 s

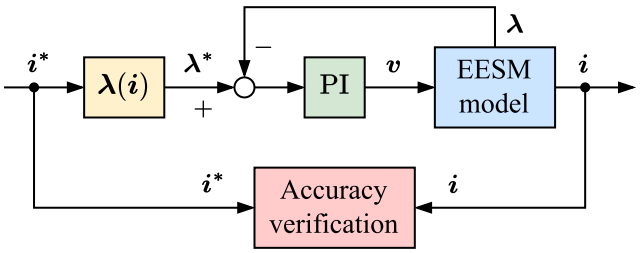


FIGURE 22. Block diagram for the accuracy verification of EESM models in simulation environment.

TABLE 3. Comparison of Simulation Run Times

Model	Run time
Current-based	3 min 48 s
Single-step flux-based	2 min 27 s
Proposed model with flux-to-current maps	2 min 41 s
Proposed model with flux-error maps	2 min 40 s
Proposed model with flux-error maps (current domain)	2 min 20 s

the partial derivatives of the fluxes as in (5) and the offline determination of $[\boldsymbol{l}(\boldsymbol{i})]^{-1}$. In the other proposed models with flux-to-current maps and with flux-error maps, most of the time is spent on performing the normalization of the stator maps domain. In this work, the required interpolation rounds for the 2-D scattered data have been performed using the MATLAB built-in function "scatteredInterpolant." However, different numerical computing environments can be adopted to implement equivalent algorithms for the interpolation of scattered data. In contrast, the single-step flux-based model requires more than one hour to be implemented, due to the long iterative search procedure. In all the considered cases, parallel computing has also been adopted to optimize the use of the available computational resources.

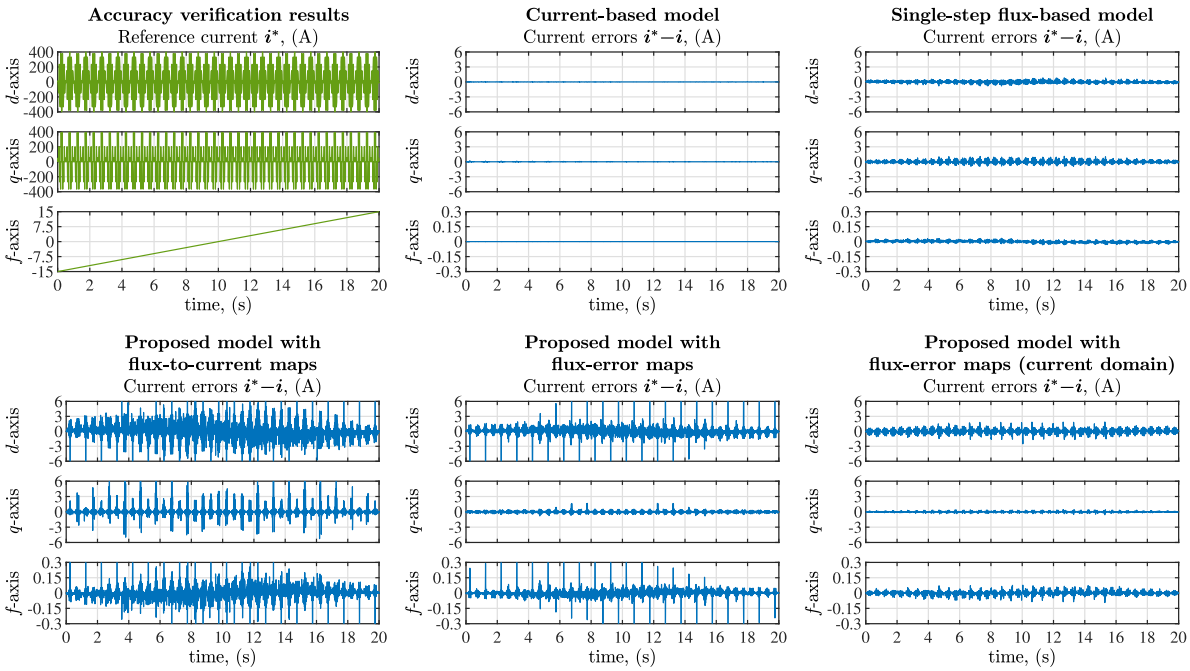


FIGURE 23. Reference current vector and results of the accuracy verification in simulation for the considered EESM CCG models.

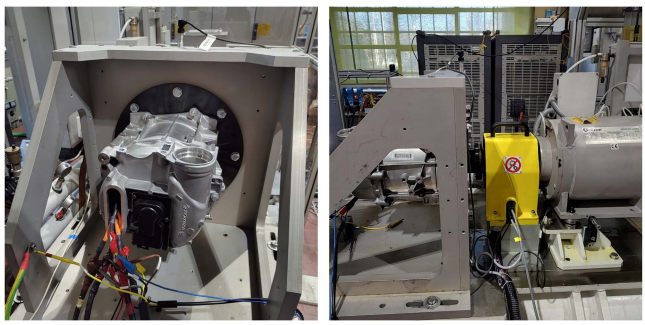


FIGURE 24. Test rig for the experimental validation: EESM under test (left), torque transducer (inside the yellow case) and driving machine (right).

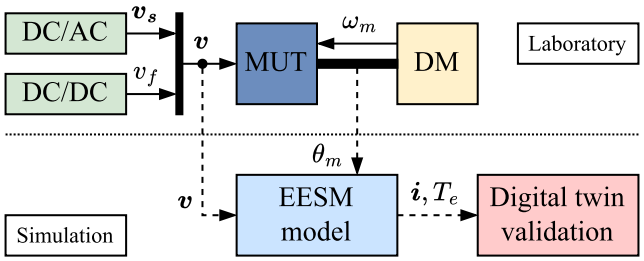


FIGURE 25. Block diagram of the digital twin tests for the experimental validation of EESM models.

B. ACCURACY VERIFICATION

The validation in simulation of the EESM models has been performed through the approach shown in Fig. 22. Arbitrary stator and rotor current references are generated by means of (38) to test many current combinations in a single numerical simulation, as presented in Fig. 23

$$\begin{cases} I_s^* = I_{s,\max} \sin(2\pi t) \\ \gamma_s^* = \pi \sin(2\pi 5t) \\ i_f^* = I_{f,\max}(0.1t - 1). \end{cases} \tag{38}$$

For (38), $I_{s,\max}$ and $I_{f,\max}$ are listed in Table 1, t is the simulation time and I_s^* and γ_s^* represent the amplitude and angle references of the stator current vector. The reference dq stator current components are therefore computed as

$$\begin{cases} i_d^* = I_s^* \cos\left(\gamma_s^*\right) \\ i_q^* = I_s^* \sin\left(\gamma_s^*\right) \end{cases} \tag{39}$$

from which $\boldsymbol{i^*} = [i_d^*;\ i_q^*;\ i_f^*]$.

The reference current vector $\boldsymbol{i^*}$ constitutes the input to the current-to-flux maps, providing the corresponding reference flux linkage vector $\boldsymbol{\lambda^*} = [\lambda_d^*;\ \lambda_q^*;\ \lambda_f^*]$, as shown in Fig. 22. By using three ideal proportional-integral (PI) regulators, the flux linkage vector $\boldsymbol{\lambda} = [\lambda_d;\ \lambda_q;\ \lambda_f]$ of the simulated model is imposed to the reference one [62].

In this framework, if $\boldsymbol{\lambda}$ and $\boldsymbol{\lambda^*}$ are the same due to the PI regulators action, then $\boldsymbol{i}$ must correspond to $\boldsymbol{i^*}$, justifying the validation mechanism presented in Fig. 22. The deviations between $\boldsymbol{i^*}$ and $\boldsymbol{i}$ characterize the correctness and accuracy of the considered model. The validation mechanism remains unchanged regardless of the considered CCG model, since only the EESM block is substituted.

The simulation results in terms of current comparisons are shown in Fig. 23. The Dormand–Prince solver has been adopted in Simulink with a maximum time step of 1 μs. In addition, the rotational speed has been set to the arbitrary value of 1500 r/min. Considering the state-of-the-art models, almost

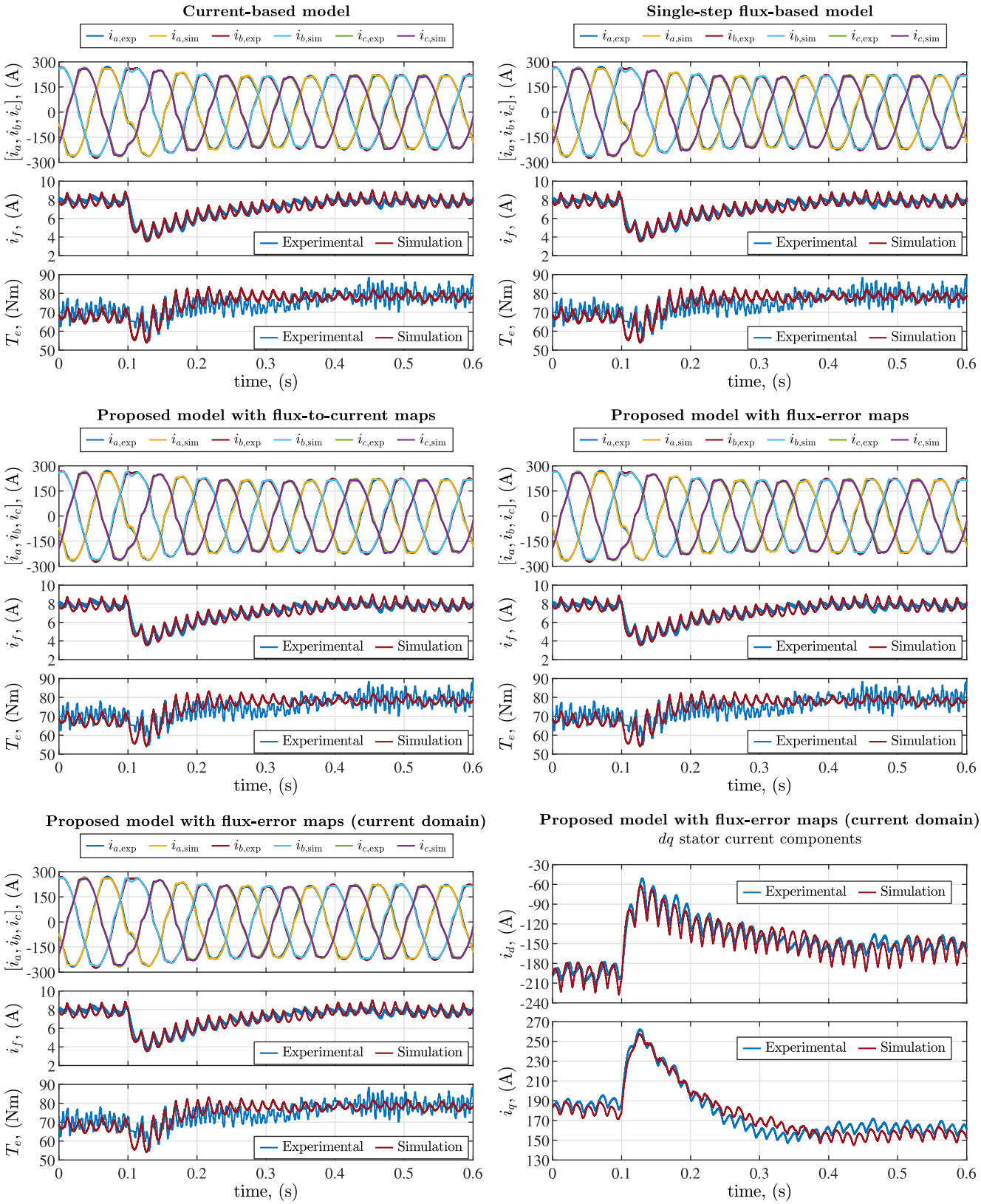


FIGURE 26. Results of the voltage steps test: comparison of experimental and simulation currents and torque for the state-of-the-art models and for the different formulations proposed for the EESM modeling with decoupled dynamics.

null current errors are obtained with the current-based one. For the single-step flux-based model, the amplitudes of the current errors are related to the tradeoff between the tolerance and the computational burden of the offline iterative search procedure [52].

With regard to the proposed EESM models, the flux-to-current and flux-error formulations achieve similar accuracy, featuring limited current errors for most of the i_d^*, i_q^*, and i_f^* combinations. The error spikes which can be seen in Fig. 23 correspond to operating points close to the boundary of the stator maps. In particular, the error spikes are observed for I_s^* larger than 98% of the maximum peak stator current for the flux-to-current formulation, and for I_s^* larger than 99% of $I_{s,\max}$ for the flux-error formulation. This issue can be solved by extending the current-to-flux maps slightly beyond the maximum peak stator current by means of experimental tests or finite element analyses, to mitigate the impact of the normalization procedure at the boundary of the stator maps.

Finally, the EESM model implemented by means of stator flux-error maps with current domain achieves high accuracy in replicating the reference currents, without producing error spikes. Indeed, the adoption of the current domain prevents the normalization procedure and scattered data interpolation in the stator maps generation, enabling limited error at the domain boundary and generally for all the current values.

In addition to the simulation results, the run times for the models are reported in Table 3. The current-based dynamic model presents the longest execution time, as it is slowed by the interpolation of the incremental inductance maps. The other models, belonging to the flux-based category, feature similar run times, thanks to the reduced number of 3-D maps involved in the simulation. It should also be considered that the values of run time are highly dependent on the time step of the numerical solver.

V. EXPERIMENTAL VALIDATION

The experimental validation of the developed CCG models has been performed by means of the same electric machine introduced in the simulation section, i.e., the 100 kW EESM sample from the Renault Zoe EV R135. In the following, the considered EESM will be referred to as machine under test (MUT) for two types of digital twin tests:

1) voltage steps;
2) torque transient.

The adoption of the term digital twin test is justified since the experimental validation provides the simulation model with voltages and mechanical rotor position measured on the MUT, to compare currents and torque with the corresponding quantities of the EESM sample.

Regarding the experimental validation setup, the MUT has been mechanically coupled to a driving machine (DM) acting as prime mover, as shown in Fig. 24. In order to acquire the torque and enable the experimental validation of the models, the torque transducer T12HP from HBK has been installed between MUT and DM.

In the voltage steps test, the MUT stator winding has been supplied by means of a silicon-carbide-based DC/AC power electronics converter connected to a 350 V bidirectional DC source, with switching frequency set to 10 kHz and dead time equal to 1 μs. Moreover, a DC/DC power electronics converter based on the insulated gate bipolar transistor (IGBT) technology has been used for the field winding supply. The corresponding switching frequency has been set to 20 kHz, with a dead time of 500 ns.

In the torque transient test, the MUT stator winding has been supplied through a DC/AC power electronics converter based on IGBT power modules, also connected to the 350 V bidirectional DC source. The switching frequency has been set to 5 kHz, with a dead time of 5 μs.

The controllers of the power electronics converters are two dSPACE MicroLabBox units, adopting sampling frequencies equal to the switching ones of the corresponding converters. In the torque transient test, the control algorithm of the drive has been developed in the MATLAB/Simulink environment with the automatic C-code generation performed by the two dSPACE controller units [30].

In addition, the electrical measurement setup consisted of current and voltage sensing during both tests. The currents of the MUT have been measured by means of high-bandwidth Hall-effect transducers IT 605-S ULTRASTAB from LEM. The PWM line-to-line voltages have been sensed by means of shielded cables connected to the high-voltage and high-resolution voltage cards GN610B from HBK GmbH. Finally, all the measurements have been sampled and stored using the calibrated transient recorder and data acquisition system GEN7tA from HBK GmbH, adopting sampling frequencies up to 2 MS/s.

For both tests, the proposed simulation models have been run by receiving the measured/reconstructed stator and rotor voltages and the mechanical rotor position as inputs. In this way, the validation of these models consisted in comparing the output currents and torque with those measured on the test rig.

A. VOLTAGE STEPS TEST

The voltage steps test allows validating the main peculiarity of the proposed EESM CCG models, consisting in separating the stator and rotor dynamics. This feature enables the stator model implementation without requiring the rotor current-to-flux map and the simulation of the rotor winding for arbitrary stator current profiles.

The block diagram of the setup for the voltage steps test is shown in Fig. 25. The DC/AC and DC/DC power electronics converters supply the stator and rotor windings, respectively, in open-loop, i.e., without current control loops. The MUT mechanical speed is imposed by the DM.

Starting from a steady-state condition, voltage steps are applied by the supply system. In particular, for this specific case, a step variation of the voltage is produced for the stator d- and q- axes, while the rotor is supplied at constant voltage. Other tests can also be performed by stepping only the rotor voltage or both stator and rotor voltages, without affecting the

validity of the proposed test. The imposed stator voltage steps allow fully assessing the effect of armature reaction on the rotor winding current.

In parallel, the reconstructed voltages and the mechanical rotor position measured on the MUT are used as inputs for the model simulation. The stator phase currents, rotor current and torque resulting from the model are compared with the corresponding measured quantities, to validate the EESM model capability to reproduce instantaneously the machine behavior. In this context, the close match between measured and simulated quantities enables the implementation of the proposed EESM CCG models with decoupled stator and rotor dynamics as valid alternatives to the available state-of-the-art current-based and flux-based models.

The voltage steps test allows also individually validating stator and rotor blocks of the decoupled-dynamics approach. Indeed, the two subsystems are separated but interdependent, and an accurate output from the rotor block requires a correct stator current input, as it can be noted in Fig. 10. The stator block behaves analogously, since the rotor current is an input.

The results of the voltage steps test are reported in Fig. 26. A MUT speed of 300 r/min has been imposed using the DM, to ensure that skin effect, iron losses and mechanical losses remain negligible during the test. The steady-state condition for the stator phase currents i_a, i_b, i_c, the i_f and the T_e prior to the stator voltage steps can be observed before $t = 0.1$ s. Specifically for the proposed EESM model based on the flux-error maps with current domain, the d- and q- stator current components are also reported for clarity.

At $t = 0.1$ s, the transient resulting from the stator voltage steps begins and the operating point of the machine moves toward the new steady-state condition, which is reached at about $t = 0.5$ s. From the results reported in Fig. 26, it can be concluded that the different formulations proposed for the decoupled-dynamics EESM models are all able to reproduce the measured quantities with high fidelity, in both the steady-state and transient conditions.

Specifically for the torque, the accuracy of all the models can be further improved by including the effects of the rotor position on the fluxes, which represents a future development of this work.

B. TORQUE TRANSIENT TEST

In order to perform an additional validation test and further demonstrate the capabilities of the proposed EESM models, both state-of-the-art and proposed models have been used to simulate an electric drive performing a fast torque transient.

In this regard, the MUT speed has been set to 500 r/min by means of the DM, to ensure that skin effect, iron losses and mechanical losses remain negligible. A torque variation has, therefore, been performed in motor mode from null torque to the peak torque of 245 N·m, at a rate of 1000 N·m/s. The torque controller used for the MUT is based on a direct flux vector control scheme, whose details can be found in [30]. As in the voltage steps test, the comparisons of stator phase currents, rotor current and torque allow validating the EESM CCG models involved in this second digital twin test.

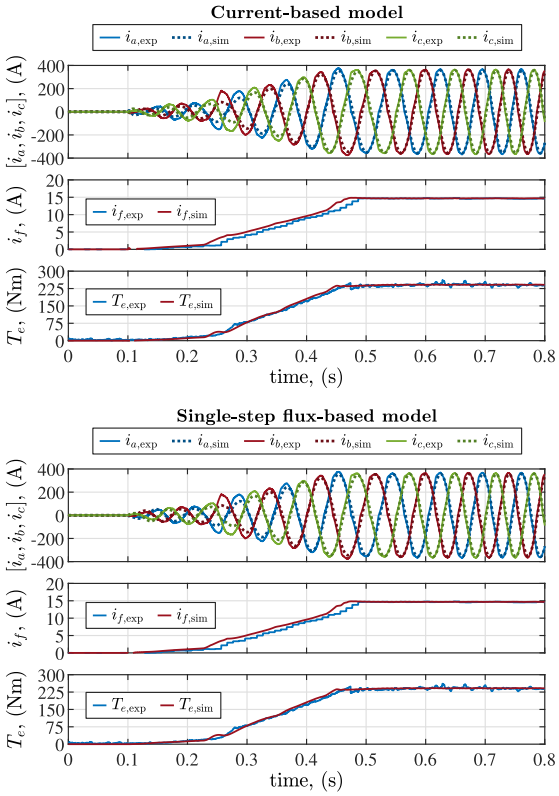


FIGURE 27. Results of the fast torque transient test for the state-of-the-art current-based and single-step flux-based models.

The results of the torque transient test are shown in Fig. 27 for the state-of-the-art models and in Fig. 28 for the different formulations of the decoupled-dynamics EESM CCG model proposed in this article.

As it can be noticed, the proposed approach enables drive simulation and control algorithm development and validation by replicating the measured MUT currents and torque, with accuracies similar to those of the state-of-the-art models. Although some deviations can be seen in the comparisons, it should be taken into account that the fidelity of the models is affected by the stator voltage reconstruction. Indeed, the input voltages of the models correspond to the reference ones imposed by the digital controllers, from which the estimated voltage errors introduced by the dead time are removed.

In this context, the large dead time (5 μs) distortion affects the stator currents accuracy, especially when their amplitude is low. Finally, the delay of the experimental rotor current with respect to that provided by the model is observed. Such delay is caused by the rotor exciter, sending the rotor current measurement with a variable delay due to the controller area network communication protocol. Nevertheless, high accuracy of the proposed EESM models is acknowledged in both transient and steady-state conditions also when they are simulated in parallel with the electric drive.

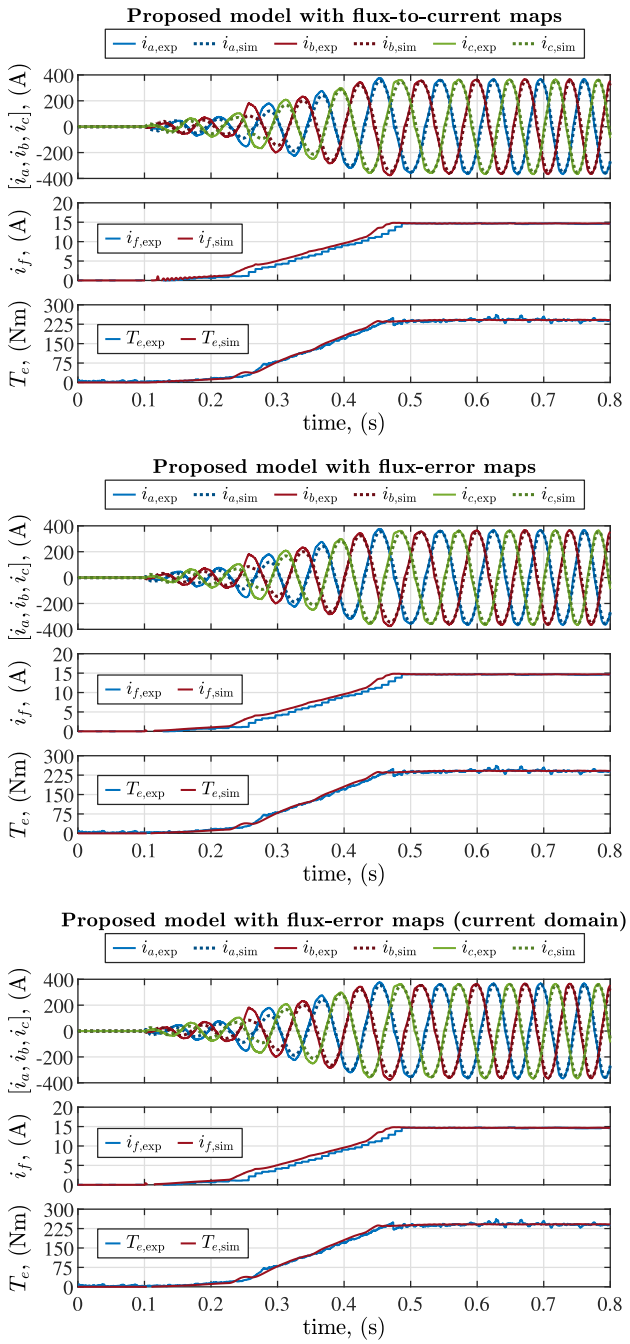


FIGURE 28. Torque transient test results for the proposed formulations of the decoupled-dynamics EESM model.

VI. CONCLUSION

This article proposed advanced EESM CCG models based on decoupled but interdependent stator and rotor dynamics. The nonlinearities introduced by the magnetic saturation are considered through multidimensional maps, derived from the machine current-to-flux relationships.

The proposed decoupled-dynamics EESM models feature enhanced simulation capabilities compared to the state-of-the-art solutions available in the literature. Indeed, the stator winding can be simulated without requiring the current-to-flux map of the rotor, while the rotor model allows evaluating the induced field winding voltage due to arbitrarily imposed stator current profiles.

Different model implementations were also presented for the decoupled-dynamics approach, providing high accuracy and low offline computational burden, as verified by means of numerical simulations. The data of an EESM sample from the Renault Zoe EV R135 have been used to verify the model implementations and to enable comparisons with the state-of-the-art formulations in the MATLAB/Simulink environment. Moreover, the model based on flux-error maps with current domain can be conveniently implemented in other simulation platforms, thanks to its straightforward formulation avoiding the domain normalization and scattered data interpolation.

The experimental validation of the proposed EESM CCG models has been performed by means of digital twin tests, by instantaneously comparing the measured currents and torque with the model output. All the tests confirmed the capability of the stator and rotor blocks in the proposed EESM models with decoupled dynamics to accurately simulate the machine. The future development of this work will consist of the following:

1) Implementation of skin effect and iron losses to model the overall EESM efficiency accurately.
2) Implementation of the dependency of flux linkages and torque on the rotor position, for accurate evaluation of spatial harmonics effects.
3) Development of EESM CCG models by means of data-driven approaches.

REFERENCES

[1] W. Liu, Y. Tao, and X. Meng, "Analysis of output characteristics of electrically excited doubly salient generator based on back EMF oriented vector control strategy," *IEEE Access*, vol. 13, pp. 53254–53265, 2025.

[2] Y. Pang, J. M. Knežević, D. Glose, and C. M. Hackl, "Sensorless control of electrically excited synchronous machines considering magnetic saturation and flux linkage dynamics for automotive applications," *IEEE Trans. Ind. Electron.*, vol. 71, no. 1, pp. 104–114, Jan. 2024.

[3] I. Boldea, L. N. Tutelea, L. Parsa, and D. Dorrell, "Automotive electric propulsion systems with reduced or no permanent magnets: An overview," *IEEE Trans. Ind. Electron.*, vol. 61, no. 10, pp. 5696–5711, Oct. 2014.

[4] S. Estenlund, M. Alaküla, and A. Reinap, "PM-less machine topologies for EV traction: A literature review," in *Proc. Int. Conf. Elect. Syst. Aircr., Railway, Ship Propulsion Road Veh. Int. Transp. Electrific. Conf.*, 2016, pp. 1–6.

[5] T. Xiao, Z. Ran, Z. Q. Zhu, D. Liang, and P. Wang, "Optimal stator/rotor copper loss ratio for maximum torque of electrically excited machines," *IEEE Trans. Ind. Appl.*, vol. 61, no. 1, pp. 137–150, Jan./Feb. 2025.

[6] F. Yao, Q. An, L. Sun, and T. A. Lipo, "Performance investigation of a brushless synchronous machine with additional harmonic field windings," *IEEE Trans. Ind. Electron.*, vol. 63, no. 11, pp. 6756–6766, Nov. 2016.

[7] F. Graffeo, S. Vaschetto, A. Tenconi, and A. Cavagnino, "Fast sizing procedure for salient-pole wound field synchronous motors for transportation electrification," in *Proc. IEEE Int. Electric Mach. Drives Conf.*, 2023, pp. 1–7.

[8] W. Bian, Z. Zhang, L. Li, C. Jin, J. Li, and F. Guo, "An approximate three-phase AC excitation method with parallel capacitors for aircraft wound rotor synchronous starter/generator," *IEEE Trans. Transport. Electrific.*, vol. 11, no. 2, pp. 5497–5508, Apr. 2025.

[9] J. Tang, Y. Liu, and N. Sharma, "Modeling and experimental verification of high-frequency inductive brushless exciter for electrically excited synchronous machines," *IEEE Trans. Ind. Appl.*, vol. 55, no. 5, pp. 4613–4623, Sep./Oct. 2019.

[10] V. Madonna, P. Giangrande, and M. Galea, "Electrical power generation in aircraft: Review, challenges, and opportunities," *IEEE Trans. Transport. Electrific.*, vol. 4, no. 3, pp. 646–659, Sep. 2018.

[11] J. de Santiago et al., "Electrical motor drivelines in commercial all-electric vehicles: A review," *IEEE Trans. Veh. Technol.*, vol. 61, no. 2, pp. 475–484, Feb. 2012.

[12] C. Rossi, D. Casadei, A. Pilati, and M. Marano, "Wound rotor salient pole synchronous machine drive for electric traction," in *Conf. Rec. IEEE Ind. Appl. Conf. 41st IAS Annu. Meeting*, 2006, vol. 3, pp. 1235–1241.

[13] D. Liang, Z. Q. Zhu, and T. Xiao, "Dynamic lumped-parameter thermal modeling for tracking maximum winding temperature in electrical machines," *IEEE Trans. Transport. Electrific.*, vol. 11, no. 4, pp. 8919–8935, Aug. 2025.

[14] Y. Liu, J. Kang, L. Sun, and T. Long, "Design and analysis of inductive power transfer system for electric machine excitation," *IEEE Trans. Transport. Electrific.*, vol. 10, no. 4, pp. 8990–8999, Dec. 2024.

[15] M. Maier and N. Parspour, "Operation of an electrical excited synchronous machine by contactless energy transfer to the rotor," *IEEE Trans. Ind. Appl.*, vol. 54, no. 4, pp. 3217–3225, Jul./Aug. 2018.

[16] D. C. Ludois, J. K. Reed, and K. Hanson, "Capacitive power transfer for rotor field current in synchronous machines," *IEEE Trans. Power Electron.*, vol. 27, no. 11, pp. 4638–4645, Nov. 2012.

[17] L. Li, Z. Zhang, W. Bian, F. Guo, Y. Yang, and J. Li, "A single-phase AC excitation method with phase-shifting capacitor for aircraft wound rotor synchronous starter/generator," *IEEE Trans. Transport. Electrific.*, vol. 11, no. 5, pp. 12300–12311, Oct. 2025.

[18] Y. Wang, S. Nuzzo, H. Zhang, W. Zhao, C. Gerada, and M. Galea, "Challenges and opportunities for wound field synchronous generators in future more electric aircraft," *IEEE Trans. Transport. Electrific.*, vol. 6, no. 4, pp. 1466–1477, Dec. 2020.

[19] J. K. Nøland, S. Nuzzo, A. Tessarolo, and E. F. Alves, "Excitation system technologies for wound-field synchronous machines: Survey of solutions and evolving trends," *IEEE Access*, vol. 7, pp. 109699–109718, 2019.

[20] N. Jiao, W. Liu, T. Meng, J. Peng, and S. Mao, "Detailed excitation control methods for two-phase brushless exciter of the wound-rotor synchronous starter/generator in the starting mode," *IEEE Trans. Ind. Appl.*, vol. 53, no. 1, pp. 115–123, Jan./Feb. 2017.

[21] A. Griffo, R. Wrobel, P. H. Mellor, and J. M. Yon, "Design and characterization of a three-phase brushless exciter for aircraft starter/generator," *IEEE Trans. Ind. Appl.*, vol. 49, no. 5, pp. 2106–2115, Sep./Oct. 2013.

[22] A. Fatima, R. Kumar, Z. Li, G. Byczynski, and N. C. Kar, "Modeling of inductances considering bar harmonics and temperature to accurately predict output torque of an induction motor," *IEEE Access*, vol. 12, pp. 156561–156571, 2024.

[23] S. Rubino, I. R. Bojoi, E. Armando, and A. Tenconi, "Deadbeat direct flux vector control of surface permanent magnet motor drives," *IEEE Trans. Ind. Appl.*, vol. 56, no. 3, pp. 2685–2699, May/Jun. 2020.

[24] J.-H. Lee, Y.-C. Kwon, and S.-K. Sul, "High-fidelity induction motor simulation model based on finite element analysis," *IEEE Trans. Ind. Electron.*, vol. 69, no. 10, pp. 9872–9883, Oct. 2022.

[25] J. S. Lee and G. Choi, "Modeling and hardware-in-the-loop system realization of electric machine drives—A review," *CES Trans. Elect. Machines Syst.*, vol. 5, no. 3, pp. 194–201, 2021.

[26] Z. Chen, D. Liang, S. Jia, L. Yang, and S. Yang, "Incipient interturn short-circuit fault diagnosis of permanent magnet synchronous motors based on the data-driven digital twin model," *IEEE Trans. Emerg. Sel. Topics Power Electron.*, vol. 11, no. 3, pp. 3514–3524, Jun. 2023.

[27] Z. Guo, S. Yan, X. Xu, Z. Chen, and Z. Ren, "Twin-model based on model order reduction for rotating motors," *IEEE Trans. Magn.*, vol. 58, no. 9, Sep. 2022, Art. no. 8206304.

[28] E. Levi and V. Levi, "Impact of dynamic cross-saturation on accuracy of saturated synchronous machine models," *IEEE Trans. Energy Convers.*, vol. 15, no. 2, pp. 224–230, Jun. 2000.

[29] E. Levi, "Saturation modelling in d-q axis models of salient pole synchronous machines," *IEEE Trans. Energy Convers.*, vol. 14, no. 1, pp. 44–50, Mar. 1999.

[30] A. Ionta, S. Rubino, F. Mandrile, F. Graffeo, R. Bojoi, and E. Armando, "Direct flux vector control of electrically excited synchronous machines for electrical vehicles," in *Proc. IEEE Energy Convers. Congr. Expo.*, 2024, pp. 6431–6438.

[31] D. C. Aliprantis, O. Wasynczuk, and C. D. Rodríguez Valdez, "A voltage-behind-reactance synchronous machine model with saturation and arbitrary rotor network representation," *IEEE Trans. Energy Convers.*, vol. 23, no. 2, pp. 499–508, Jun. 2008.

[32] A. M. Cramer, B. P. Loop, and D. C. Aliprantis, "Synchronous machine model with voltage-behind-reactance formulation of stator and field windings," *IEEE Trans. Energy Convers.*, vol. 27, no. 2, pp. 391–402, Jun. 2012.

[33] D. Aliprantis, S. Sudhoff, and B. Kuhn, "A synchronous machine model with saturation and arbitrary rotor network representation," *IEEE Trans. Energy Convers.*, vol. 20, no. 3, pp. 584–594, Sep. 2005.

[34] D. Aliprantis, S. Sudhoff, and B. Kuhn, "Experimental characterization procedure for a synchronous machine model with saturation and arbitrary rotor network representation," *IEEE Trans. Energy Convers.*, vol. 20, no. 3, pp. 595–603, Sep. 2005.

[35] S. Pekarek, E. Walters, and B. Kuhn, "An efficient and accurate method of representing magnetic saturation in physical-variable models of synchronous machines," *IEEE Trans. Energy Convers.*, vol. 14, no. 1, pp. 72–79, Mar. 1999.

[36] K. Corzine, B. Kuhn, S. Sudhoff, and H. Hegner, "An improved method for incorporating magnetic saturation in the q-d synchronous machine model," *IEEE Trans. Energy Convers.*, vol. 13, no. 3, pp. 270–275, Sep. 1998.

[37] S.-A. Tahan and I. Kamwa, "A two-factor saturation model for synchronous machines with multiple rotor circuits," *IEEE Trans. Energy Convers.*, vol. 10, no. 4, pp. 609–616, Dec. 1995.

[38] A. Ionta, S. Rubino, F. Graffeo, and R. Bojoi, "High-fidelity voltage-behind-reactance model of electrically excited synchronous machines using flux maps," *IEEE Open J. Ind. Appl.*, vol. 6, pp. 603–618, 2025.

[39] X. Chen, J. Wang, B. Sen, P. Lazari, and T. Sun, "A high-fidelity and computationally efficient model for interior permanent-magnet machines considering the magnetic saturation, spatial harmonics, and iron loss effect," *IEEE Trans. Ind. Electron.*, vol. 62, no. 7, pp. 4044–4055, Jul. 2015.

[40] A. Bojoi, S. Ferrari, P. Pescetto, and G. Pellegrino, "Advanced circuital model for e-drive simulation, including harmonic effects and fault scenarios," in *Proc. PCIM Eur. 2023; Int. Exhib. Conf. Power Electron., Intell. Motion, Renewable Energy Energy Manage.*, 2023, pp. 1–10.

[41] H. Le-Huy and P. Brunelle, "A versatile nonlinear switched reluctance motor model in Simulink using realistic and analytical magnetization characteristics," in *Proc. 31st Annu. Conf. IEEE Ind. Electron. Soc.*, 2005, pp. 1556–1561.

[42] S. Li, D. Han, and B. Sarlioglu, "Modeling of interior permanent magnet machine considering saturation, cross coupling, spatial harmonics, and temperature effects," *IEEE Trans. Transport. Electrific.*, vol. 3, no. 3, pp. 682–693, Sep. 2017.

[43] M. Boesing, M. Niessen, T. Lange, and R. De Doncker, "Modeling spatial harmonics and switching frequencies in PM synchronous machines and their electromagnetic forces," in *Proc. 20th Int. Conf. Elect. Mach.*, 2012, pp. 3001–3007.

[44] C. Kukura, J. Apsley, and S. Djurović, "Computational features of electric machine hybrid FEA-DQ dynamic models," *IEEE Access*, vol. 12, pp. 120116–120130, 2024.

[45] D. Hu, Y. M. Alsmadi, and L. Xu, "High-fidelity nonlinear IPM modeling based on measured stator winding flux linkage," *IEEE Trans. Ind. Appl.*, vol. 51, no. 4, pp. 3012–3019, Jul./Aug. 2015.

[46] Y. Kano, K. Watanabe, T. Kosaka, and N. Matsui, "A novel approach for circuit-field-coupled time-stepping electromagnetic analysis of saturated interior PM motors," *IEEE Trans. Ind. Appl.*, vol. 45, no. 4, pp. 1325–1333, Jul./Aug. 2009.

[47] G. Weidenholzer, S. Silber, G. Jungmayr, G. Bramerdorfer, H. Grabner, and W. Amrhein, "A flux-based PMSM motor model using RBF interpolation for time-stepping simulations," in *Proc. Int. Electric Mach. Drives Conf.*, 2013, pp. 1418–1423.

[48] S.-W. Su, C. M. Hackl, and R. Kennel, "Analytical prototype functions for flux linkage approximation in synchronous machines," *IEEE Open J. Ind. Electron. Soc.*, vol. 3, pp. 265–282, 2022.

[49] B. Jiang, J. Tang, and Y. Liu, "Extended-Kalman-filter-based field current estimation for brushless electrically excited synchronous machines using stator current measurements," *IEEE Trans. Transport. Electrific.*, vol. 11, no. 1, pp. 5042–5054, Feb. 2025.
[50] J. Tang, B. Jiang, H. Chen, Y. Liu, and S. Lundberg, "Dynamic current reference determination of electrically excited synchronous machines based on torque gradients of copper losses," *IEEE Trans. Power Electron.*, vol. 39, no. 6, pp. 7423–7433, Jun. 2024.
[51] P. G. Carlet, L. Cinti, L. Ortombina, and N. Bianchi, "Dynamic model for HEPM motors including the nonlinear magnetic characteristics," in *Proc. IEEE Int. Electric Mach. Drives Conf.*, 2023, pp. 1–7.
[52] L. Geier, J. Stoß, A. Liske, and M. Hiller, "Generalized inversion of n-dimensional flux maps for unified nonlinear machine models and predictive control algorithms," in *Proc. IEEE Energy Convers. Congr. Expo.*, 2023, pp. 4821–4828.
[53] L. Perilli, F. Graffeo, S. Rubino, and S. Vaschetto, "Dynamic models for electrically excited synchronous machines based on flux-to-current and current-to-inductance maps," in *Proc. IEEE Energy Convers. Congr. Expo.*, 2024, pp. 5588–5595.
[54] S. Wendel, P. Karamanakos, A. Dietz, and R. Kennel, "Flux linkage-based model predictive current control for nonlinear PMSM drives," in *Proc. IECON 46th Annu. Conf. IEEE Ind. Electron. Soc.*, 2020, pp. 3051–3056.
[55] L. Ortombina, F. Tinazzi, and M. Zigliotto, "Magnetic modeling of synchronous reluctance and internal permanent magnet motors using radial basis function networks," *IEEE Trans. Ind. Electron.*, vol. 65, no. 2, pp. 1140–1148, Feb. 2018.
[56] S. Rubino, L. Tolosano, F. Mandrile, E. Armando, and R. Bojoi, "Flux polar control (FPC): A unified torque controller for AC motor drives," *IEEE Trans. Ind. Appl.*, vol. 59, no. 4, pp. 4140–4163, Jul./Aug. 2023.
[57] C.-M. Ong, *Dynamic Simulation of Electric Machinery: Using Matlab/Simulink*. Englewood Cliffs, NJ, USA: Prentice-Hall, 1997.
[58] L. Perilli, F. Graffeo, S. Rubino, A. Tenconi, and S. Vaschetto, "Modular dynamic model for multi-three-phase electrically excited synchronous machines," in *Proc. IEEE Energy Convers. Congr. Expo.*, 2025, pp. 1–8.
[59] A. El-Serafi, A. Abdallah, M. El-Sherbiny, and E. Badawy, "Experimental study of the saturation and the cross-magnetizing phenomenon in saturated synchronous machines," *IEEE Trans. Energy Convers.*, vol. 3, no. 4, pp. 815–823, Dec. 1988.
[60] E. Armando, R. I. Bojoi, P. Guglielmi, G. Pellegrino, and M. Pastorelli, "Experimental identification of the magnetic model of synchronous machines," *IEEE Trans. Ind. Appl.*, vol. 49, no. 5, pp. 2116–2125, Sep./Oct. 2013.
[61] S. Goehner et al., "Combining locked rotor and steady state tests for eesm flux linkage identification," in *Proc. IEEE 9th Southern Power Electron. Conf.*, 2024, pp. 1–6.
[62] H. A. A. Awan, S. E. Saarakkala, and M. Hinkkanen, "Flux-linkage-based current control of saturated synchronous motors," *IEEE Trans. Ind. Appl.*, vol. 55, no. 5, pp. 4762–4769, Sep./Oct. 2019.



LORENZO PERILLI (Student Member, IEEE) received the B.Sc. degree in industrial engineering from Università degli Studi dell'Aquila, L'Aquila, Italy, in 2020, and the M.Sc. degree in electrical engineering from Politecnico di Torino, Torino, Italy, in 2023.

He is currently working toward the Ph.D. degree in electrical engineering with the Department of Energy "G. Ferraris," Politecnico di Torino.

His research activities include design, modeling and analysis of conventional and superconducting electric machines for high-power aircraft electrification.



SANDRO RUBINO (Senior Member, IEEE) received the M.Sc. and Ph.D. degrees in electrical engineering from Politecnico di Torino, Torino, Italy, in 2014 and 2019, respectively.

He is currently an Associate Professor with the Energy Department "G. Ferraris," Politecnico di Torino. He is involved in many research projects with industry aimed at technology transfer from academia. His research activities include modeling and controlling multiphase electrical machines and high-performance motor drives.

Dr. Sandro Rubino is currently the Secretary of the Industrial Drive Committee (IDC) of the IEEE Industry Applications Society (IAS). He is also an Associate Editor for IEEE TRANSACTIONS ON INDUSTRY APPLICATIONS and IEEE JOURNAL OF EMERGING AND SELECTED TOPICS IN POWER ELECTRONICS. He was the recipient of four paper awards from IAS-IDC and two Ph.D. thesis awards for the design and validation of advanced torque controllers for traction and propulsion motors.



FEDERICA GRAFFEO (Member, IEEE) received the B.Sc. degree in energy engineering from Università degli Studi di Palermo, Palermo, Italy, in 2017 and the M.Sc. and Ph.D. degrees in electrical engineering from Politecnico di Torino, Torino, Italy, in 2020 and 2023, respectively.

She is currently an Assistant Professor with the Energy Department "G. Ferraris," Politecnico di Torino. Her research interests include the electromagnetic and thermal design of synchronous electrical machines for transportation applications, with a particular focus on wound-field synchronous motors.

Dr. Graffeo is currently a Reviewer for several IEEE Transactions and international conferences.



SILVIO VASCHETTO (Senior Member, IEEE) received the M.Sc. and Ph.D. degrees in electrical engineering from the Politecnico di Torino, Italy, in 2007 and 2011, respectively.

He then joined ABB IEC LV Motors Technology Center, Vittuone, Italy, as R&D Engineer. From 2012 to 2014, he was with Magna Electronics Italy, as Electromagnetic Simulation and Motor Design Engineer. He is currently a Professor with the Energy Department "G. Ferraris," Politecnico di Torino. His research interests include electromagnetic design, thermal analysis, and energetic behavior of electrical machines for transportation and high-performance applications.

Dr. Vaschetto is currently an Associate Editor for IEEE TRANSACTIONS ON INDUSTRY APPLICATIONS, IEEE TRANSACTIONS ON ENERGY CONVERSION, and Special Issues Editor for IET *Electric Power Applications Journal*.



ALBERTO TENCONI received the M.Sc. and Ph.D. degrees in electrical engineering from the Politecnico di Torino, Torino, Italy, in 1986 and 1990, respectively.

From 1988 to 1993, he was with the Electronic System Division, FIAT Research Center, where he was engaged in the development of electrical vehicle drive systems. He then joined the Department of Electrical Engineering (now Energy Department), Politecnico di Torino, where he is currently Head of Department. His research activity is documented by more than 200 papers published in International Journals and International Conferences. He has participated, both as a designer and as scientific responsible, in many National and European Research Programmes. His current research interests include electric machines, power converters, and drives for transportation electrification.

Dr. Tenconi is currently a Reviewer for International Journals and has been an Associate Editor for the TRANSACTIONS ON INDUSTRIAL ELECTRONICS.